Characterization of Optically Sensitive Amorphous Selenium Photodetector for Indirect X-Ray Imaging

by

Saeedeh Ghaffari

A thesis
presented to the University of Waterloo
in fulfillment of the
thesis requirement for the degree of
Master of Applied Science
in
Electrical and Computer Engineering

Waterloo, Ontario, Canada, 2014

I hereby declare that I am the sole author of this thesis. This is a true copy of the thesis, including any required final revisions, as accepted by my examiners.

I understand that my thesis may be made electronically available to the public.

Abstract

Advances in medical imaging have significantly improved patient care, and considering all modalities X-ray imaging is historically the pioneer. Recently, there has been an ongoing interest in development of large area digital X-ray systems with possible advantages including improvement of image quality and dose efficiency. Amorphous selenium (a-Se) is one of the most highly developed photoconductors used in digital X-ray imaging (direct and indirect conversion) where it has been adapted from use in xeroradiographic photoreceptors. One of the challenges associated with a-Se based photodetectors is high dark current at applied electric fields $> 10V/\mu m$ due to the injection of charge carriers (mainly holes), which can be resolved by introducing hole and electron blocking layers.

The primary focus of this research is to investigate different aspects of a-Se based photodetectors with polyimide (PI) as a hole blocking layer. In order to achieve the most efficient device, the dark (I_{dark}) and photo (I_{ph}) responses for different thicknesses of PI (varied from $0.4\mu m$ to $2.5\mu m$) have been studied. The photoconductivity ratio (I_{ph}/I_{dark}) suggests that the sample with $1\mu m$ PI has the best response in the high electric field region of operation ($> 10V/\mu m$). Further, in order to find the exact electric field within the a-Se in the PI/a-Se structure, time of flight (TOF) measurements have been carried out for different thicknesses of PI. Based on the TOF measurements, the electric field within the PI layer has to reach $138V/\mu m$ to provide good conduction. Moreover, the hole mobility of $0.11cm^2/V.s$ at $12.8V/\mu m$ electric field for a-Se has been calculated, which is consistent with the previously reported results.

Another aspect of a detector which is critical in high frame rate imaging applications is temporal performance (lag and ghosting). In this study, the time dependence of dark current after illumination at different temperatures and under various electric fields has been investigated. Based on the results and the proposed theoretical model, the lag behaviour in

a-Se photodetectors depends on inherent properties such as the density of trapped states (holes) and the hole release time constant. According to our fitted model, the hole de-trapping time constant has been found to be 26 and 170 sec at room temperature with a calculated trapped hole density of 1.25x10^{11} m^{-3} and 3.4x10^{10} m^{-3} at 10V/μm electric field. These values correspond to the existence of different interface defect states for holes in the bulk of a-Se.

Finally, the temperature stability and durability of the a-Se photodetector with PI has been investigated to determine the extent to which the device can handle environmental stresses (high temperature) during transportation and storage. Comparing the photo and dark responses of the device before and after stress indicates no significant degradation, which implies a contribution of PI to the reliability of the a-Se photodetector.

Acknowledgements

I would like to express my deepest thanks to my supervisor, Dr. Karim S. Karim, for his continued support, positive attitude and advice during the course of this degree.

I am deeply indebted to my parents, Soodabeh and Keramat, who provided the much needed encouragement for success. Thank you for your love, support and unwavering belief in me. Many thanks to my sisters and brothers for always bringing a smile to my face.

Much of the work in this thesis could not have been completed without the efforts of other individuals and their help is greatly appreciated. Special thanks to Shiva Abbaszadeh for all her advice and valuable help. I am grateful to Sina for his love and countless support, I could not have done it without you.

Lastly, I would like to thank my friends scattered over the world who proved that true friendship knows no distance.

Dedication

To my parents, Soodabeh and Keramat, for their love, support, and love again.

Table of Contents

List of Tables

List of Figures

Chapter 1

Introduction

Advances in medical imaging have significantly improved patients care in the past two decade and among all common procedures, X-ray imaging is the pioneer. Since 1895, the X-ray discovery has opened a new phase in medical diagnostic as it captures images of things that are invisible to the naked eyes, such as broken bones. The X-ray employs a variety of energy sources to penetrate the body's tissue and produce useful images. For instance, the typical energy range of the incident X-rays phtons for diagnostic purposes are $20 - 120KeV$. The classification of X-ray based on its energy is summarized in table 1.1 [1].

Table 1.1: X-ray classification [1]

Application	Energy range (KeV)	Wavelength (Å)
Low-energy	0.1-20	124-0.62
Diagnostic-range X-rays	20-120	0.62-0.1
Orthovoltage X-rays	120-300	0.1-0.04
Intermediate-energy X-rays	300-1000	0.04-0.01
Megavoltage X-rays	$>$ 1MeV	$<$ 0.01

1.1 Conventional X-ray Imaging

Due to the vital impact of X-ray imaging on medical diagnosis, there has been a huge improvement in X-ray imaging field since X-ray discovery. The first method of X-ray imaging was film-screen technology. In this method the X-ray film is attached to an intensifying screen, due to the low absorption efficiency of X-ray film in the medical diagnostic range $(20 - 120KeV)$. The image was then developed using a chemical tank in the dark room. Although this method has improved the medical diagnosis tremendously, it has several drawbacks, including: X-ray films storage and transportation difficulties, lack of real-time imaging, and huge chemical wastes [11].

A common technique of X-ray imaging which allows real-time imaging is image intensifier. As it is shown in figure 1.1, this technique employs a photocathode (Sb_2S_3) to convert visible light to electrons, a high vacuum tube to accelerate the electrons, and a phosphor film attached to a charge couple device (CCD) for video monitoring. Although this technique has the benefit of real-time imaging with a low dose exposure, the image quality is relatively low and the manufacturing and maintenance costs are considerably high [12].

Another widely used X-ray imaging technique is computed radiography (CR). CR uses an imaging plate instead of X-ray films, and provides the image in a digital format which has resolved the storage problems related to X-ray films. This method is similar to film screening, expect instead of developing the image in a chemical tank at dark room, the imaging plate is scanned by a red laser to transfer the data in a digital format to a computer. This technique does not provide instant images and real time imaging.

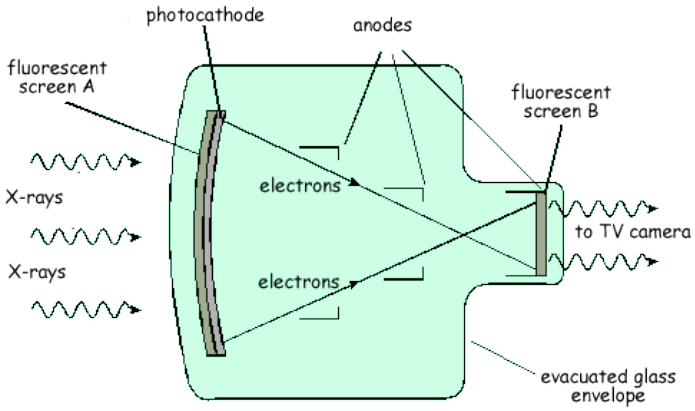

Figure 1.1: Image intensifier schematic

1.2 Digital Flat Panel Imaging

Recently, there has been an ongoing interest in developing digital X-ray systems. One of the most important aspects of transition from analog to digital is the improved image quality by image processing, which allows low dose imaging. Further, the storage of the data into a computer eliminates the issues associated with the X-ray films and the image is available immediately. Digital flat panel X-ray imagers, as the most promising technique for radiography, are consists of two main components: an X-ray detector and a readout circuit. The readout circuit can be based on either a passive pixel sensor (PPS) or an active pixel sensor (APS) technology. The two main methods of x-ray detection used in flat panel detectors are: direct and indirect conversion [13, 14]. Direct flat panel detectors employ a photoconductive material, such as a-Se to convert the X-ray photons directly into the electrical charges as it is shown in figure 1.2. On the other hand, indirect flat panel detectors use a scintillator to interact with the X-ray photons and convert them into visible light, and then the light is converted into electrical charges by photodiodes (figure

1.2) [3]. Compared with the screen films and the computed radiography, both direct and indirect detectors have a better image quality. At present, flat panel detectors mostly rely on indirect conversion method, however direct conversion is a promising method and has several advantages, including higher spatial resolution [15–18]. In the direct conversion process, the lateral spreading of the generated charge carriers is minimal due to the uniform electric field across the photoconductor, while the indirect conversion detectors suffer from light scattering leading to an image blurring [19]. In addition to the higher image quality, the direct conversion detectors have a simpler structure, so that their manufacturing process is considerably simpler and cheaper [20, 21]. Temporal artifacts and dark current problem in some photoconductive materials as a result of high bias are the drawbacks of direct conversion detectors [22]. Good progress has been made to improve the properties of direct conversion detectors and there are ongoing researches in this field to develop an ideal X-ray imaging detector.

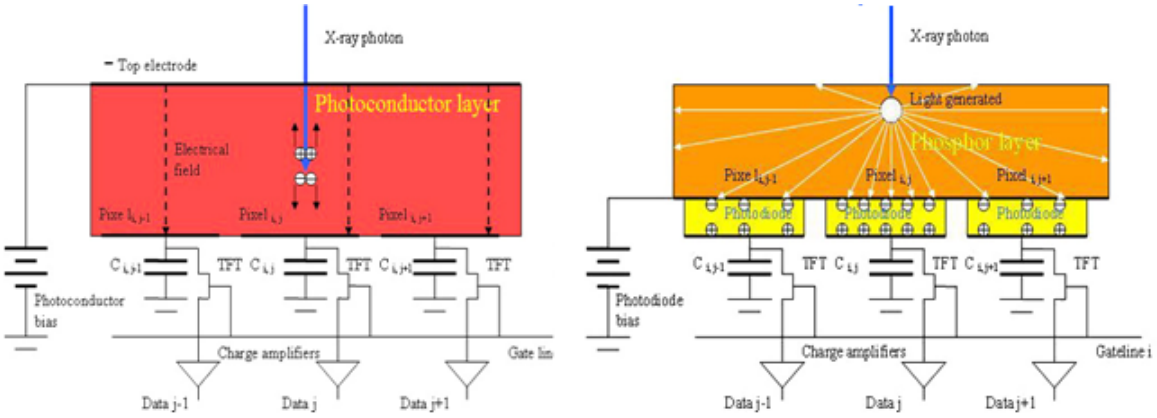

Figure 1.2: Schematic of direct conversion detector (left), and indirect conversion detector(right) [4].

1.2.1 Indirect Conversion Detector

In the indirect detection a scintillating phosphor is used to convert the incident X-ray photons into light as it is shown in figure 1.2. So far, the most commonly used phosphors in flat-panel detectors are Gd_2O_2S:Tb and CsI:Tl [23]. The typical materials used as scintillator for X-ray medical imaging applications are demonstrated in table 1.2 along with their physical properties.

Table 1.2: Physical properties of typical scintillator used for X-ray medical imaging applications [2].

Material	Density (g/cm^3)	Maximum emission(nm)	Light yield (photons/Mev)	Decay time(ns)	Afterglow (% after 3ms/100ms)
CsI:Tl	4.51	550	66000	800 - >6000	>2/0.3
CsI:Na	4.51	420	40000	630	
$CaWO_4$	6.1	420	20000		
Gd_2O_2S:Tb:Tb	7.3	545	60000	10^6	
$CdWO_4$	7.9	495	20000	5×10^3	<0.1/0.02

An ideal scintillator should have a high light yield, which is defined as N_{ph}/E_{x-ray}, where N_{ph} is the number of optical photons produced by an incident X-ray photon, and E_{x-ray} is the amount of energy of the incident X-ray photon. Other properties for an ideal scintillator are: fast response, good spectral matching with photodetector, and minimal light spreading [24–26]. The visible light is then converted into electrical charges using photodetectors, such as p-i-n photodiode integrated to one pixel. The p-i-n photodiode has the benefit of uniform large area deposition, however the fabrication process is complicated and it requires expensive manufacturing facilities. The amount of photogenerated charges

is proportional to the intensity of light emitted from the phosphor in the region near the pixel. As discussed before, indirect conversion detectors suffer from light scattering and some photons from adjacent pixels are detected by the photodetectos, which decreases the spatial resolution. This can be partially solved using a structured phosphor such as Cesium Iodide (CsI), which acts as a fibre-optic light guide [23]. Some desirable properties of an ideal photodetector are listed below:

- High conversion gain
- Low dark current
- Fast response time
- Possibility of low cost and large area fabrication
- Compatibility with TFT or CMOS processes

High signal collection efficiency in the indirect detection process is achieved by increasing the geometrical fill factor of the photodiodes or instead employing a photoconductive material capable of operating in avalanche mode. The latter approach is observed in a-Se photoconductor which makes it a good candidate to replace the p-i-n photodiode [27].

1.2.2 Direct Conversion Detector

The selection and a design of the photoconductor are the two important factors that critically depend on the performance of direct conversion detectors. The properties of an ideal photoconductor are listed below:

- $\delta << L$, where δ is the absorption depth of the x-rays, and L is the photoconductor thickness. This criteria should be met, so that most of the incident X-ray photons are absorbed within a photoconductor thickness, and unnecessary patient exposure is avoided. Photoconductors with a high density and atomic number are desirable, since they have a larger absorption coefficient. However, phtoconductors with low atomic numbers should be thicker to absorb the X-ray photons efficiently.

- $W_{\pm}$ should be as low as possible, where $W_{\pm}$ is the electron hole pair (EHP) creation energy, which is related to the energy gap E_g of a material [28].

- The dark current should be as small as possible to increase the dynamic range and reduce the noise. Depending on the clinical application, the dark current is preferred to be in the range of 10-1000 pA/cm2 [29].

- There should be a slight amount of deep trapping of the generated electrons and holes within the bulk to get an artifact-free image.

- The lateral spreading of the generated charges should be as small as possible to achieve a high spatial resolution.

- The possibility of low cost manufacturing process and uniform large area deposition of the photoconductor layer should also be taken into account.

- The photoconductor properties should not change or deteriorate with time as a consequence of repeated exposure to x-rays, i.e. the photoconductor should be stable and reliable.

Despite amorphous selenium's success as an X-ray photoconductor in the clinical imaging application, there are still active researches on other potential photoconductors, such

as HgI_2, PbI_2, PbO, and CdZnTe [30]. In a-Se devices the value of $W_{\pm}$ is about $50eV$ under typical operating electric field ($10V/\mu m$), where the $W_{\pm}$ value is almost ten times smaller ($5-6eV$) for polycrystalline mercuric iodide (poly-HgI_2) and polycrystalline Cadmium Zinc Telluride (poly-CdZnTe) [4]. On the other hand, polycrystalline sensors' main drawbacks are higher dark current, image lag, and non-uniform responses due to the large grain sizes. Some efforts have been done to improve the quality of the mentioned photoconductors, and it appears that HgI_2 is a good replacement for a-Se. Recent studies on HgI_2 show low dark current and good charge transport properties at reasonable applied fields [29].

1.3 Thesis Outline

The primary focus of this research is to investigate different aspects of the a-Se based photodetector with a hole blocking layer. One of the challenges associated to the a-Se based photodetector is a high dark current at the electric field of $> 10V/\mu m$ due to the injection of carriers (mainly holes), which can be resolved by introducing hole and electron blocking layers. The PI(hole blocking layer)/a-Se structure has been previously reported by our research group, which demonstrated a low dark current in the electric field region of interest. Chapter 2 begins with the study of fundamental properties of the a-Se photodetector, followed by the investigation of different thicknesses of PI (varied from $0.4\mu m$ to $2.5\mu m$) to achieve the best performance out of the photodetector and thus optimize the PI thickness. Further, in Chapter 3 the exact voltage drop across a-Se film, which has not been quite known within the PI/a-Se structure, is discussed. This is important since the mobility of the charge carriers and the photogeneration efficiency in a-Se are strongly dependent to the electric field across a-Se film. Hence, the exact behaviour of polyimide layer under

various electric fields and at the presence of photogenerated carriers in the a-Se film should be studied. To address the above question, time of flight measurement is carried out on different thicknesses of PI. Another aspect of the detector is the temporal performance, which is critical in real time imaging. In order to have a better insight of lag behaviour of the PI/a-Se photodetector, the dark current after illumination (turn-off dark current) at different temperatures and under various applied voltages is studied in Chapter 4. The results from these measurements are in agreed to a model that we propose for the turn-off dark current of PI/a-Se structure. Chapter 5 investigates the temperature stability of the photodetector, to see how well this device can handle the environmental stress (high temperature) during its transportation and storage. Further, the durability of the device as a consequence of repeated light exposures over a year is studied by comparing its previous and recent dark and photo responses. The conclusions from the experimental results are presented in Chapter 6 along with contributions of this thesis to the field of amorphous selenium technology.

Chapter 2

Amorphous Selenium as a Photoconductor

2.1 Introduction

To date, amorphous selenium is one of the most well known photoconductors used in the photocopying industry and the clinical X-ray imaging. The fundamental properties and characteristics of amorphous selenium will be discussed in this chapter, followed by the essential requirements that a-Se-based photoconductor should meet. Further, the optimized structure which leads to a higher value of photoconductivity ratio will be studied.

2.2 Amorphous Selenium Atomic Structure

Amorphous selenium's physical properties are studies by looking at the atomic structure and the atomic distribution. Selenium with an atomic number of 34 is a member of group

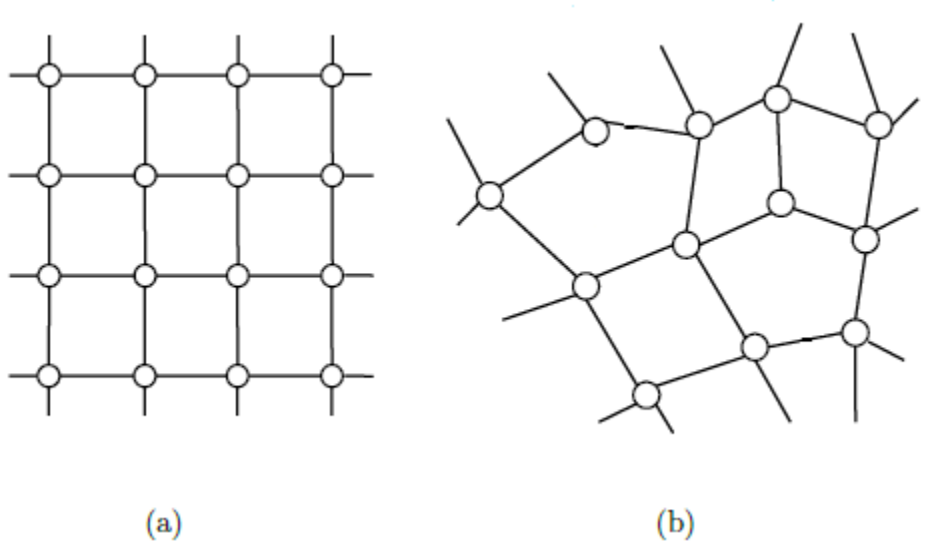

Figure 2.1: Atomic structure of a crystalline semiconductor where the coordination of bonding is four (a), and an amorphous semiconductor; where it has under-coordination (b).

VI (called chalcogens) of the periodic table. In a-Se twenty eight electrons occupy the inner shell; two electrons in the outer shell occupy the 4s subshell, and the rest occupies the 4p subshell. The two 4s-electrons form a lone pair as well as two electrons in 4p, and they do not participate in the bonding. The remaining two electrons are available for the formation of covalent bonds with other atoms, leading to the two-fold coordinated bonds with an optimum angle of 105° [31]. Selenium exists in both crystalline and amorphous forms. Unlike crystalline selenium where the atoms are distributed periodically, amorphous selenium has a random atomic lattice structure. Figure 2.1a shows the atomic structure of a crystalline semiconductor (coordination number of four), where the bond length and bond angles are identical, and the solid posses a long-range order. However, in the atomic network of the amorphous semiconductor, the bond length and the bond angles are not identical for each atom necessarily. As it is shown in figure 2.1b, the long-range order is

lost, but the amorphous semiconductor exhibits some short-range orders. Some atoms have coordination other than four, called the structural defects, and they introduce additional localized states in the electronic structure of amorphous material. Similarly, the structural defects occur in a-Se lattice, leading to the creation of localized defect states in its energy gap.

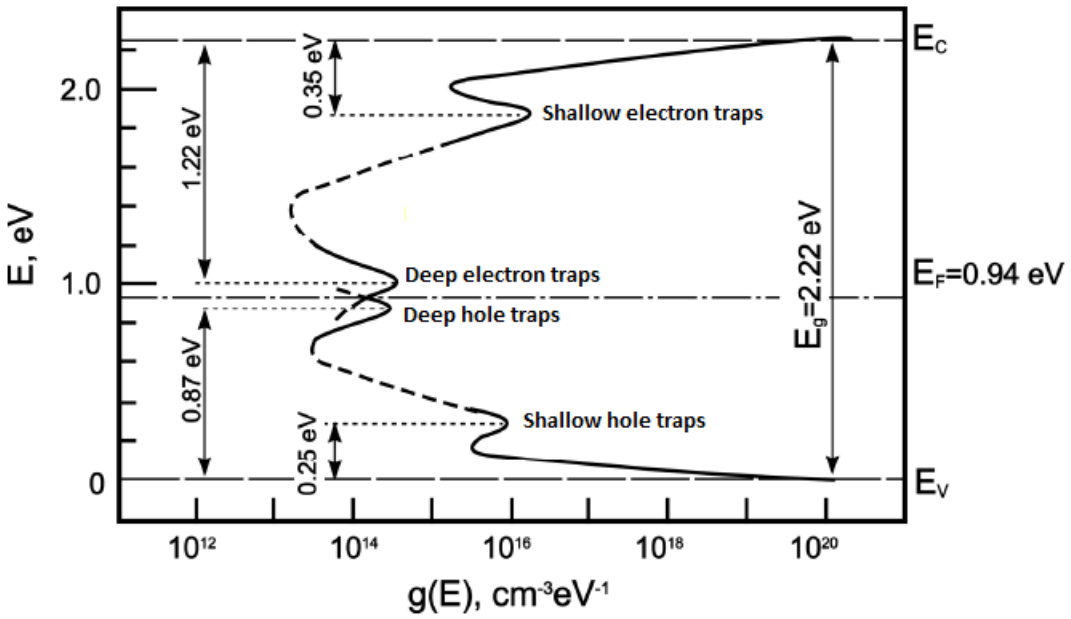

Figure 2.2: Density of states in amorphous selenium proposed by Abkowitz [5].

Due to the presence of long-range disorder in amorphous materials the density of state (DOS) of these materials are more complicated than crystalline materials. The current accepted model for a-Se density of state was proposed by Abkowitz in 1988 which was derived from time of flight, xerographic cycled up residual voltage decay, and the xerographic dark discharge measurements [5]. Figure 2.2 shows the DOS of a-Se, where in addition to the extended states, there are four sets of defect states within the bandgap of a-Se. The two

defect states near the valence and conduction band-edges are referred as shallow traps for holes and electrons respectively. Shallow traps controls the carrier drift mobility [32]. On the other hand, the two defect states near the Fermi level are related to the deep defects for holes and electrons, which control the carrier life time in a-Se film. It should be noted that pure a-Se is not thermally stable and it crystallizes over time. However, a-Se alloyed with about $0.2 - 0.5\%$ As prevents crystallization [28]. This process introduces more deep hole traps, thus reduces the hole life time. In order to improve the hole transport, the alloy is doped with $10 - 20ppm$ Cl (called stabilized a-Se). By adjusting the amount of As and Cl, both holes and electrons can drift in a-Se and contribute to its photoconductivity.

2.3 a-Se-Based Photoconductor Figures of Merit

Amorphous selenium is one of the most highly developed photoconductors that has been used in the photocopying industry and medical X-ray imaging for decades. In 1959, Xerox Corporation introduced the first commercial office copier, Xerox 914, and revolutionized the document-copying industry. The photocopier used a $50 - 60\mu m$-thick a-Se film as a photoreceptor, coated on an Al drum. Later, they developed Xerox 125 medical imaging system, using a stabilized $125\mu m$-thick a-Se, vacuum coated onto the oxidized Al plates [3]. Amorphous selenium has some features that makes it a good X-ray photoconductor. For instance, the amorphous selenium film can be deposited simply in large area with a good uniformity. This aspect is important, since X-ray cannot be focused, and to get an image of the human body the detector should be larger than the body part. Further, amorphous selenium is easily coated up to the thickness of $1000\mu m$ for the direct conversion X-ray imaging, which is able to absorb the X-ray photons efficiently, although it has a low atomic number in compared with other X-ray photoconductors. It also can be used in the indirect

X-ray detection due to its band gap and high sensitivity to the blue light (wavelength of 468nm) [10]. In the following subsections, the a-Se photoconductor's figures of merit will be discussed.

2.3.1 Dark Current

In the absence of radiation, a relatively small current that flows through a photocundoctor under the influence of electric field is called dark current. High dark current increases the electrical shot noise and reduces the dynamic range, which limits the smallest detectable signal. Moreover, during the flow of dark current the charges can be trapped in the a-Se bulk, which changes the internal electric field and thus affects the photogeneration efficiency [33]. Therefore, it is important for the detector to have a negligible amount of dark current, i.e. in the range of 1 pA/mm^2 for clinical x-ray imaging application [3,34,35]. Dark current may consist of two major components in the a-Se based photoconductor including:

- thermal generation of the free carriers in the a-Se film
- injection of carriers from electrodes in to the a-Se bulk.

It is believed that, at the electric field of $< 10\ V/\mu m$, the dominant component of the dark current is the injection of carriers from the metallic contact, also the thermal generation is negligible due to the large mobility gap of a-Se film (2.2 eV) [5,36]. However, the generation of charge carriers from localized states in the bandgap of the a-Se can be enhanced exponentially at higher electric fields as result of thermally assisted tunnelling effect, called Poole-Frenkel effect [37]. The thermal generation rates for holes and electrons are calculated as below [38,39].

$$g_h = N(E_{qF})kT\upsilon_0 exp[-(E_{qF} - E_V - \Delta\Phi)/kT], \tag{2.1}$$

$$g_e = N(E_{qF})kT\upsilon_0 exp[-(E_C - E_{qF} - \Delta\Phi)/kT], \tag{2.2}$$

where $N(E_{qF})$ is the density of states at energy of E_{qF} in the midgap of a-Se, υ_0 is the attempt to escape frequency (typically $10^{12}s^{-1}$), E_V and E_C are the valence and conduction band edges, and $\Delta\Phi$ is the reduction in the potential energy of the barrier due to the PooleFrenkel effect. $\Delta\Phi$ is equal to $\beta_{pf}\sqrt{F_0}$, where $\beta_{pf} = \sqrt{e^3/\pi\varepsilon}$ is the Poole-Frenkel coefficient, and $\epsilon = \epsilon_0\epsilon_r$ is the permittivity of a-Se [40,41]. The thermal generation current can be calculated as equation 2.3, if we assume all the thermally generated carriers are collected.

$$I_{th} = egAL, \tag{2.3}$$

where A is the area and L is the thickness of a-Se. Practically some of the thermally generated carriers will re-trapped before being collected and thus the thermal generation current modifies and can be written as [42]:

$$I_{th} = egA\mu\tau F[1 - \frac{\mu\tau F}{L}(1 - exp(\frac{-L}{\mu\tau F}))], \tag{2.4}$$

where μ is the carrier mobility and τ is the carrier life time of a-Se film.

Several studies have been carried out to understand the origin of the dark current in the metal/a-Se/metal structure, but a general dark current mechanism have not concluded for the mentioned structure [36,43]. Majority of reported studies in sixties and seventies claim that a steady state dark current was observed and it was explained in terms of Space Charge

Limited Current (SCLS) [44, 45]. However, the a-Se film's typical dark current is less than their observed levels of dark current. Other researchers have shown that the dark current was limited by a potential barrier, called Schottky barrier [46]. Johanson et al. studied the effect of different metallic contacts on the a-Se film evaporated on an ITO glass; the work function of selenium was larger than all the metals that have been studied, and the ITO contact was grounded. Their results show no correlation between the dark currents and the work function of the metal contacts, which implies that the dark current does not follow the Schottky emission model. They reported that the dark current behaviour strongly depends on the nature of the interface between the metal and a-Se [36]. Further, based on their data from time of flight measurement, they have concluded that the dark current in a-Se film do not obey SCLC. On the other hand, they have shown that, while the ITO contact was positively biased, the I-V curves for all the samples were similar. Therefore, it can be concluded that the dominant conduction mechanism in metal/a-Se/metal structure is due the hole injection from the positively biased electrode rather than the electron injection from the negatively biased electrode. This can be explained by considering that the $\mu_h\tau_h$ is larger than $\mu_e\tau_e$ by one order of magnitude in a-Se film [3]. Recently Kabir et al. developed an analytical model for the transient and steady state dark current in a-Se based detector with a hole blocking layer. The model is considering the hole injection from the metal electrode and the thermal generation, and they have found a good agreement between the experimental data and theoretical model [47]. As a consequent of believing that the dominant component of the dark current is the carrier injection, there have been a lot of efforts in reducing the dark current by adding a thin blocking layer between the a-Se and the electrodes which is going to be discussed more in the following sections.

2.3.2 Optical Properties

An incident photon with a certain energy can be absorbed by the photoconductor, and then can create electron-hole pairs (EHPs). The fraction of the incident photons that are absorbed by the photoconductor depends on the thickness and absorption coefficient of the photoconductor. If we assume that no photons are reflected from the surface, the number of the absorbed photons by the material is in the form of $(1 - e^{-\alpha L})P_{in}/h\upsilon$, where L is the thickness, α is the absorption coefficient, h is the Planck constant, and υ is the frequency of incident photons. The absorption coefficient depends on the atomic number and density of the photoconductor, and the energy of the incident photons. If the energy of the incident photon is less than the band gap of a-Se, the absorption coefficient is extremely small. However, this value rises rapidly as the energy of the incident photon increases to the value of the bandgap. In the presence of the electric field the photogenerated carriers can be separated before being recombined. Photogeneration efficiency or internal quantum efficiency (η_{int}) is defined as the number of EHPs that escaped recombination (EHP) divided by all the generated EHPs. Majority of studies were carried out to define the a-Se photogeneration mechanism in 1970s. Based on their results, it was shown that the η_{int} of a-Se depends on the applied electric field, photon energy, and temperature. The most widely used approach to describe this dependency is the Onsager theory [6].

Figure 2.3 shows the experimental data for photogeneration efficiency of a-Se film as a function of applied electric field for various wavelength of excitation source [6]. The solid lines are the theoretical Onsager dissociation efficiencies for $\Phi_0 = 1$ (efficiency of production of thermalized EHPs per absorbed photon), and the initial separation (r_0) as indicated in the figure. The experimental data shows that the photogeneration efficiency of a-Se film increases by decreasing the wavelength of light, and for shorter wavelength

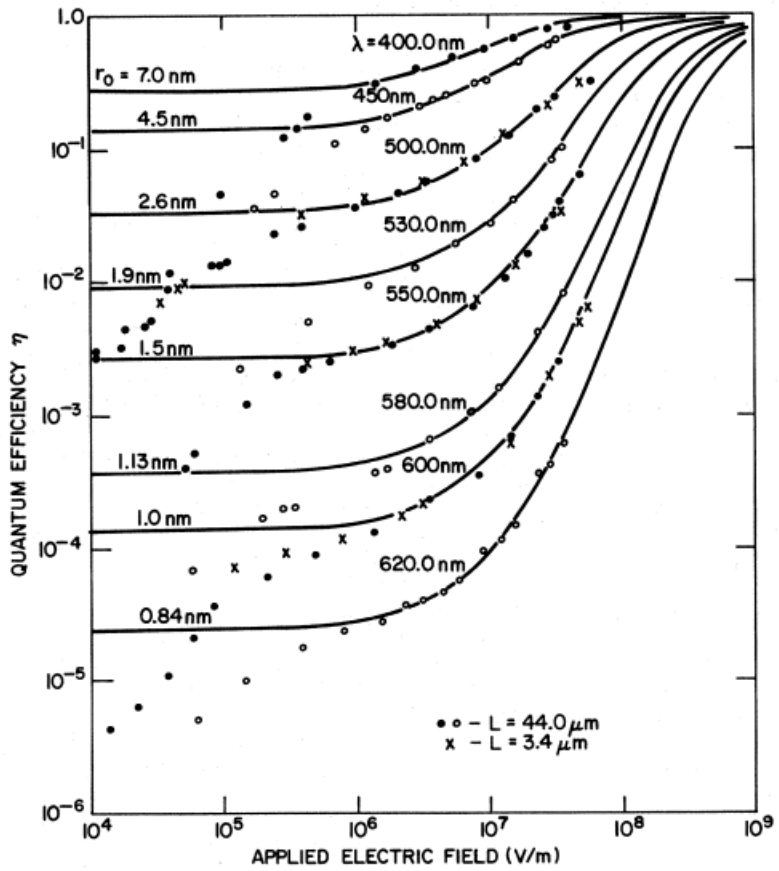

Figure 2.3: Experimental data for photogeneration efficiency of a-Se film with two different thicknesses as a function of applied electric field, and for various exciting wavelength of light (circles and crosses). The solid lines are the theoretical Onsager dissociation efficiencies for $\Phi_0 = 1$, and for initial separation r_0 as indicated in the plot [6].

excitation the value becomes closer to unity at the electric field of $> 10^7 V/m$. Further, for longer wavelength although the photon energy is greater than the a-Se bandgap, due the smaller initial distance between the generated EHPs the dissociation efficiency is smaller which leads to a lower quantum efficiency.

2.3.3 Charge Transport

As discussed, both shallow and deep traps exist in the a-Se film, and they control the carrier mobility and lifetime respectively. It should be noted that in order to achieve a high collection efficiency, the average distance that a charge drifts before being trapped in the deep trapping state should be much larger than the thickness of the photoconductor. This distance, called carrier Schubweg, depends on the applied electric field, mobility and carrier lifetime ($\mu\tau F$) [48]. Time of flight (TOF) and Interrupted-Field Time-of-Flight (IFTOF) techniques are used to measure the carrier mobility and carrier life time [49]. The detailed principles of the TOF is explained in chapter three. The transport properties of the stabilized a-Se derived from the mentioned techniques are shown in table 2.1. Considering the electric field of $10V/\mu m$ across stabilized a-Se, the carrier Schubweg for hole and electron are calculated as $1300\mu m$ and $400\mu m$ respectively. These values are much longer than the typical thickness of a-Se film, so that a high collection efficiency is achievable. For instance, for a-Se based mammographic detectors with the thickness of $200\mu m$, the collection efficiency of the X-ray generated charges is close to unity (98%) [3].

2.3.4 Temporal Response

Temporal imaging characteristics can be categorized into two main components, known as lag and ghosting. Lag is the carry-over of the signal from the previous X-ray exposure, and ghosting is described as a change in the sensitivity or gain of the detector as a result of previous X-ray exposure. It has been found that bulk trapping within the detector causes both lag and ghosting [50]. Figure 2.4 demonstrate the lag and ghosting effects after an exposure over a circular area. As it is shown in figure 2.4 b, the trapped charges from the previous exposure over the circular area are released thermally, leading to an increase in

Table 2.1: The transport properties of stabilized a-Se film (a-Se alloyed with $0.2-0.5\%$ As and $10-40ppm$ Cl) [3]

Property	Value	$\mu\tau F$ at$10V/\mu m$	Comment
$\mu_h(cm^2/V.s)$	0.13-0.14	-	Independent of thickness and source of a-Se,very reproducible
$\tau_h(\mu s)$	50-500	1300 μm	Depends on the substrate temperature and impurities
$\mu_e(cm^2/V.s)$	2-4$\times$ 10^{-3}	-	Depends on the source of a-Se and As content
$\tau_e(\mu s)$	200-1000	400 μm	Depends on impurities, independent of the substrate temperature, increases with As content

the dark image (lag). Moreover, the trapped charges in the bulk can induce more injection from the contacts and contributes to lag [43, 51]. Figure 2.4c, shows the effect of ghosting on the sensitivity of the detector, where the trapped charges from the previous exposure over the circular area recombine with the generated charges in the subsequent exposure, and thus reduce the sensitivity [52, 53]. Further, the gain is also affected by the change in the electric field distribution as consequence of trapped charges in the bulk [54]. It should be noted that the trapped electrons contribute more than trapped holes in ghosting. This can be explained by the DOS of a-Se (figure 2.2), where the deep hole trapping state exists $0.9eV$ above the valence band, and the deep electron trapping state distribution is $1.2eV$ below the conduction band. Therefore, the average release time for trapped electrons is longer than trapped holes. Lag and ghosting can be a major issue in low dosage and high frame rate modalities such as fluoroscopy. The combination of material properties, system design and operational parameters should be taken into account to reduce the temporal artifacts (lag and ghosting) [54].

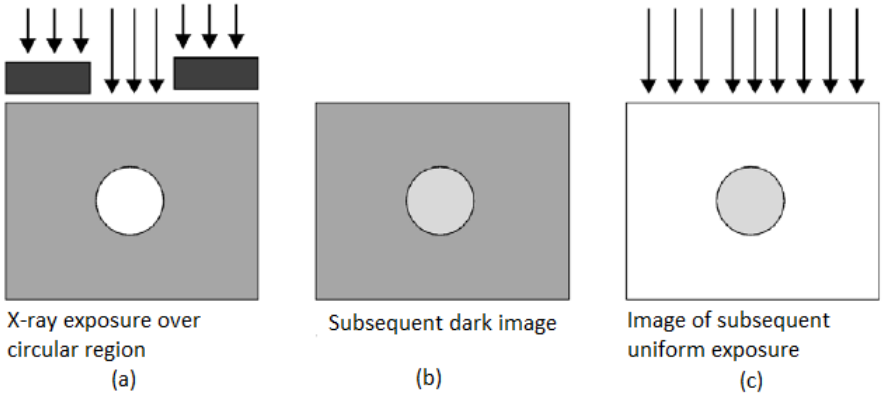

Figure 2.4: Demonstration of lag and ghosting after an exposure over a circular area. (a)Exposure over the circular area. (b) Dark image immediately after the exposure is increased due to release of trapped charges. (c) Shadow of the previous exposure is visible in the image of the subsequent exposure (adapted from [7]).

2.3.5 Avalanche Mode

The avalanche multiplication in an a-Se-based photoconductor was first observed by Juska et al. [55]. They discovered that at electric field of about $> 80\ V/\mu m$, the effective quantum efficiency was larger than unity. It was found that at high electric fields the primary charge carriers (holes) acquired enough energy to produce secondary EHPs, which attributed to impact ionization and avalanche multiplication [56]. The avalanche multiplication mechanism in low mobility amorphous semiconductor has been recently explained in terms of lucky drift model [57]. In order to get the avalanche gain, high electric field is applied across the a-Se film, leading to high injection of carriers from the electrodes, which is not desirable. This was resolved by using proper electron and hole blocking layers within the a-Se photoconductor to prevent high injection of carriers. High-gain Avalanche Rushing Photoconductor (HARP) TV camera tubes, was developed as a first practical application of avalanche multiplication, which can produce an avalanche gain of around 10^3. The

Harp tube structure consists of a-Se film doped with arsenic and tellurium, sandwiched between the hole blocking (CeO_2) and electron blocking (Sb_2S_3) layers [58]. The readout mechanism in Harp device needs a vacuum tube, which is suitable for large area imaging (bulky size). The avalanche multiplication of a-Se photoconductor is an important feature which can provide sufficient gain for low-dose, large-area imaging applications by further improvement of the structure.

2.4 a-Selenium-Based Photodetector with a Blocking Layer

As discussed in the previous section, the acceptable range of dark current of the detector for clinical x-ray imaging applications is $1-10\ pA/mm^2$, which cannot be achieved with a simple metal/a-Se/metal structure under high operating electric field region ($> 10V/\mu m$). This was resolved by developing the a-Se detector with a multilayer structure to block electron and hole injection from the electrodes [59]. The dominant component of the dark current in a-Se photoconductors is the hole injection from the positively biased electrode. Therefore, a proper hole blocking layer should be placed in between the anode and a-Se film, which has the following properties [10]:

- It creates a large potential barrier for holes or consists of a large number of hole traps and a very low hole mobility
- Permits the flow of electrons
- Low cost and compatible with the large area electronics semiconductor fabrication process.

At present, one of the technologies to manufacture the a-Se direct conversion flat panel imagers with blocking contacts is the use of p-like and n-like doped layers of selenium, as an electron and hole blocking layers respectively (established by Anrad company) [60]. This technology has long term stability issues and the properties of the i-layer changes due to the drifting of dopant ions into the intrinsic layer at high electric fields ($> 10V/m$) [61]. Another technology is the use of parylene as a hole blocking layer and an undisclosed electron-blocking layer, which is not appropriate for real time imaging due to the existence of charge accumulation at the interface of parylene and a-Se (established by Hologic company) [62].

Abbaszadeh et al. studied different hole blocking materials to achieve an a-Se photodetector with a high conversion gain. They have tested two inorganic ($Ce0_2$ and TiO_2) and two organic materials (PTCBI and PI) within $16\mu m$-thick a-Se. It was found that using $800nm$-thick PI layer results in a lower dark current at higher electric fields region in compared with CeO_2 ($30nm$), TiO_2 ($20nm$), or PTCBI ($50nm$) [10]. Figure 2.5 demonstrates the effect of polyimide layer on the dark current reduction by comparing the dark response of the $15\mu m$-thick a-Se film with $2\mu m$-thick PI and without PI. It can be seen that in PI/a-Se structure, the dark current is increasing by increasing the applied voltage upto $981V$, which is still lower than the dark current of a-Se-only structure under $10V/\mu m$ electric field. Moreover, lag improvement in PI/a-Se structure has been reported previously, while ghosting was degraded due to the extremely low dark current (below $10pA/mm^2$) [63]. From figure 2.5, the lag improvement is also noticeable by observing the low dark current in PI/a-Se device after illumination in compared with a-Se only device. It should be noted that the same photocurrent is achieved for the two structures by increasing the applied voltage upto $981V$ for the a-Se/PI structure, while the dark current before and after illumination for PI/a-Se device is kept as low as the acceptable range of dark current for

medical imaging applications. Therefore, this structure is promising, but the polyimide thickness should be optimized. It should be thick enough to keep the dark current as low as possible, and at the same time it should not be too thick, so that the voltage drop across a-Se is sufficient to achieve a high photogeneration efficiency. The device fabrication and optimization of polyimide layer are discussed in the following subsections.

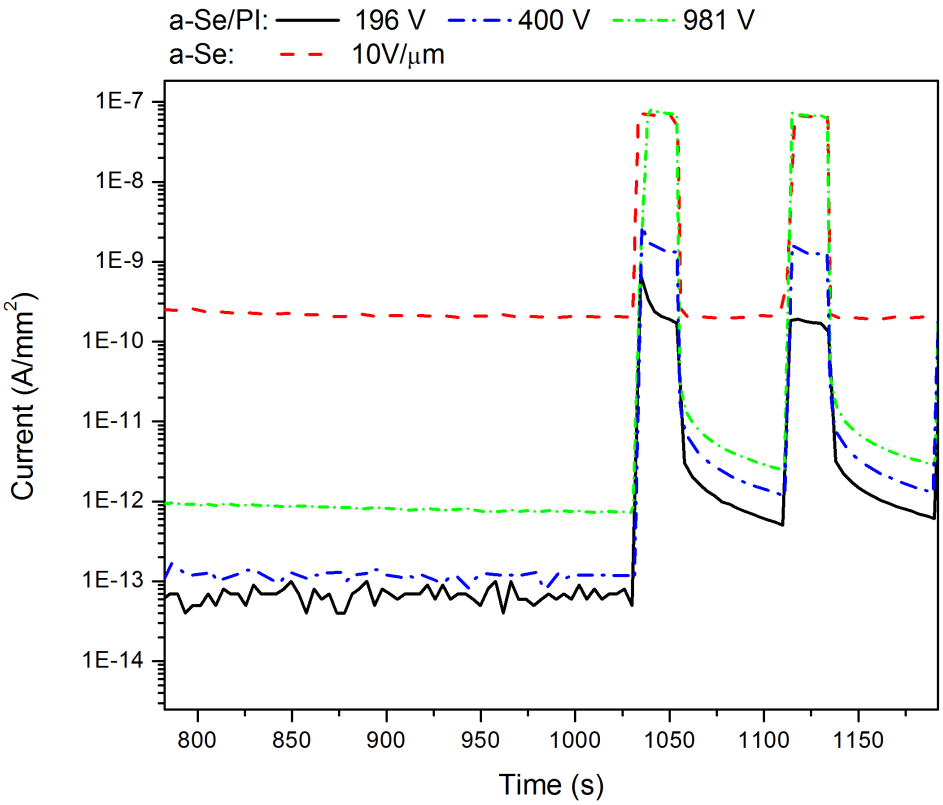

Figure 2.5: Photo and dark current measurement of the a-Se photodetector with and without blocking layer. The thickness of polyimide layer is 2 μm and the a-Se thickness is 15 μm.

2.4.1 Device Fabrication

The devices under study have been fabricated at University of Waterloo. Figure 2.6 shows the device structure. In our process as a bottom electrode, we have employed indium tin oxide (ITO) coated glass slides which has been demonstrated to have 85 percent transparency in visible range [10]. The fabrication process can be summarize into four main steps including:

Substrate cleaning: The ITO coated glass is cleaned and washed through ultrasonic bath with acetone and propanol (IPA) followed by DI water rinsing and nitrogen drying.

Polyimide spin coating: The thickness of spin coated polyimide is defined by the viscosity of the polyimide solution, as well as the speed of spinning, and the duration of curing. In this research we have used the least viscose polyimide solution available commercially (PI 2610 by HD-MicroSystem). Further, in order to get a thin polyimide film ($\sim 400nm$), we have diluted the polyimide solution with N-Methyl-2-pyrrolidone (NMP). The detailed process specification of PI spin coating is shown in table 2.2.

Table 2.2: Polyimide spin coating process specification

PI Thickness (μm)	PI solution	Spinning speed (kRPM)	Soft bake 1 at $90°C$	Soft bake 2 at $150°C$	Hard curing at $350°C$
0.4	PI 2610 (diluted)	5	$90s$	$90s$	30 min
1	PI 2610	5	$90s$	$90s$	30 min
1.8	PI 2610	3	$90s$	$90s$	30 min
2.5	PI 2610	2	$90s$	$90s$	30 min

Amorphous selenium: $15\mu m$ a-Se has been deposited with thermal evaporation system

at University of Waterloo (Giga2Nano Lab). In order to get a high mobility a-Se film, the evaporation has been carried out at substrate temperature of $65°C$ with deposition rate of $100\mathring{A}/sec \pm 10$ at pressure of $1 \times 10^{-8} torr$, and then the substrate has cooled down for more than 10 hours. The quality and reproducibility of the a-Se film has been thoroughly investigated and reported by Dr. Abbaszadeh [7].

Gold deposition: Gold has been used as a top electrode, since it permits low carrier injection to the a-Se [36]. A $40nm$-thick gold has been deposited with thermal evaporation system (separate from a-Se thermal evap.) with the rate of $8-15\mathring{A}/sec$ at the pressure of below $2 \times 10^{-6} torr$. The top electrode has been formed using a shadow mask to skip any photo-lithography step. The area of the in-house fabricated device varies from $1mm^2$ to $36mm^2$.

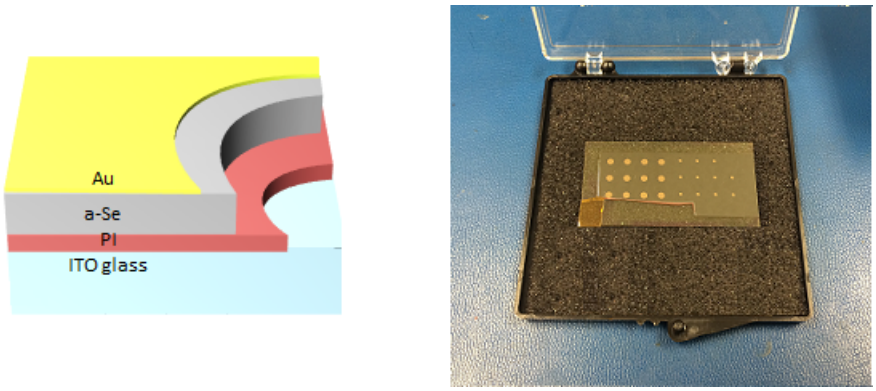

Figure 2.6: Amorphous selenium based photodetector structure (left), in-house fabricated device (right) .

2.4.2 Optimized Polyimide film as a Hole Blocking Layer

In order to optimize the PI layer for the a-Se-based photodetector, different thicknesses of PI layer (0.4 μm to 2.5 μm) with the same thickness of a-Se (16 μm) were fabricated. The PI/a-Se film was sandwiched between ITO glass (anode) and Au (cathode). Beside, one device without PI was fabricated as a reference. The dark and photo current transient behaviour of each device under different biasing voltages was tested. From the results of the measurements the effect of PI thicknesses on the dark and photo performance of the PI/a-Se detector was investigated. Table 2.3 shows the specification of the samples prepared for this study. As it was discussed in the previous section, polyimide film acts as a hole blocking layer, but flows the electrons freely above specific electric field. Th blocking layer reduces the injection of holes from the ITO contact, so that the device is able to function at high electric fields.

Table 2.3: Samples prepared for optimization of PI layer

Sample #	PI Thickness (μm)
S1	0
S2	0.4
S3	1
S4	1.8
S5	2.5

It should be noted that if the PI layer does not conduct efficiently (due to a low electric field or degradation) while the device is illuminated by light, the photo generated electrons are going to accumulate at the interface of PI and a-Se films. These trapped charges reduce the electric field across a-Se film, which results in the decrement of the amplitude of the photocurrent. The photocurrent of the samples at 300 V applied voltage is shown in figure 2.7. Both photocurrent of the consequent pulses are in the same range which states no

charge build up (trapped electrons) occurs at the interface of the PI and a-Se films. If we consider all the photogenerated electrons are trapped at the interface of PI/a-Se, the electric field across a-Se will reduce dramatically after only 500 ms of light exposure (468 nm light source, intensity of 170 $\mu W/cm^2$) [7]. However, in our experiment the light pulse width was more than 30 s and the photocurrent did not decrease significantly.

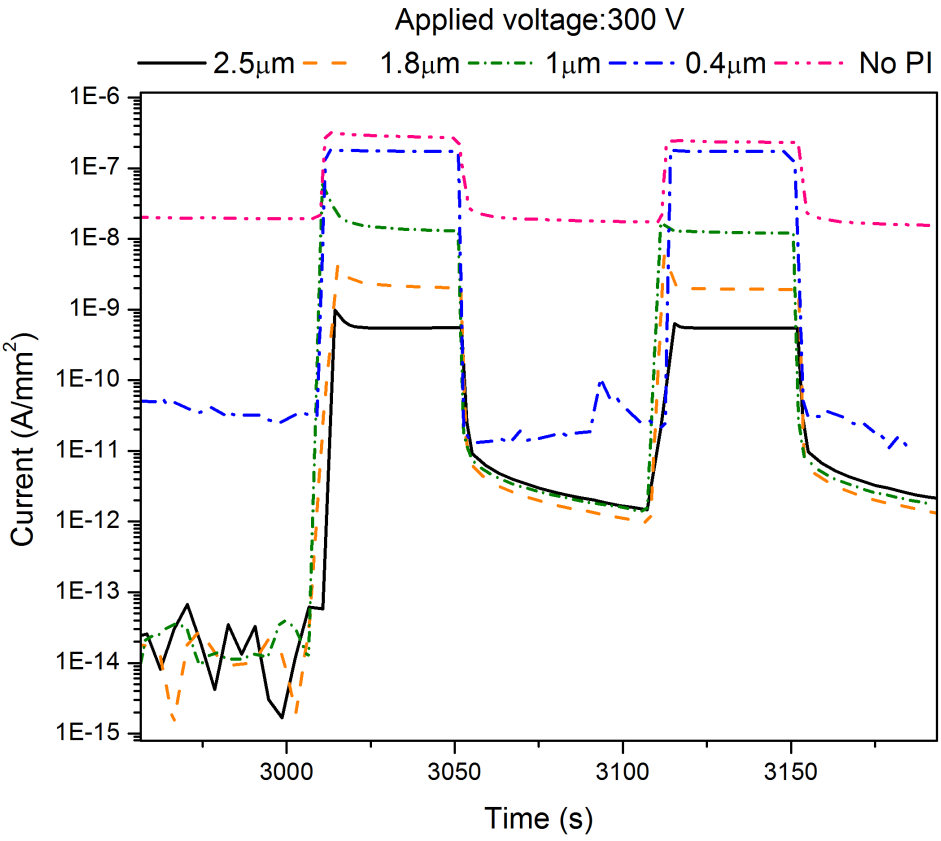

Figure 2.7: Electrical conduction current of the a-Se-based photodetector with different thicknesses of PI at 300 V applied voltage. The samples were exposed by a 468 nm wavelength source with the intensity of 128 $\mu W/cm^2$.

The device was rested for 3000 s under dark condition at 300 V, and the dark current became stable for all the samples. It can be seen in figure 2.7 that the stable dark current

is more than two order of magnitude for sample S1 in compared to S2. This huge deviation in the dark current is due to the high carrier injection from the anode electrode in sample S1. As a result of introducing a thin blocking layer ($400nm$), the dark current was reduced significantly, which shows that the carrier injection is a major component contributing to the dark current of the device. It is noticeable that the dark current after illumination (turn-off dark current) increases by two orders of magnitude in compared with the the dark current before illumination (stable dark current) for sample S3, S4, and S5. However, for sample S1 and S2 we do not observe a significant difference between the stable and the turn-off dark current. This is related to the dominant component of dark current before and after illumination in each structures. As it was discussed before, dark current in photoconductor stems from three major sources including:

- Thermal generation
- Carrier injection from electrodes (mostly hole in case of amorphous selenium)
- Detrapping of trapped carriers after illumination.

Regarding dark current which is measured after $3000s$ resting (stable dark current), the major components of dark current is thermal generation and carrier injection. For sample S3, S4 and S5, since thick PI layer has been used in between the anode and a-Se film, the only component that contributes to the stable dark current is thermal generation which is in consistent with the calculated thermal generation dark current shown in the previous section. In contrasts, sample S1 and S2 shows higher dark current which expresses that the major component of stable dark current is the carrier injection. On the other hand, in addition to the thermal generation and carrier injection, detrapping of trapped carriers plays a major role in turn-off dark current. In case of thick PI samples (S3, S4 and S5),

the dominant component of the turn-off dark current is detrapping of trapped chargers, which explains the difference of stable dark current and turn-off dark current. However, in sample S1 and S2, the detrapping of trapped chargers is negligible in compared with the carrier injection. Therefore, we do not expect to observe huge difference between the stable dark current and turn-off dark current for sample S1 and S2. More analysis has been carried out regarding turn-off dark current behaviour in chapter four.

The photocurrent of the samples during illumination and turn-off dark current of the samples at a specific time and under various applied voltages are measured and shown in figure 2.8. It is noticeable that the photocurrent is decreasing by introducing the blocking layer, and as we increased the thickness of the blocking layer the photocurrent decreased more under the same applied voltage. This is obviously due to the reduction of voltage drop across a-Se film. In order to get a same photocurrent in a device with a thicker PI layer and sample S1, we increased the applied voltage. For instance, sample S1 under 150 V and sample S2 under 300 V applied voltages have almost the same photocurrent. In the presence of light, the conductivity of a-Se layer increases, which leads to an increase in the voltage drop across the PI layer and improves the conduction of electrons within the PI layer. To calculate the voltage drops across a-Se and PI films we considered the partial resistance of the films. The thicker the PI layer, the lower the voltage across a-Se film. Hence, the photo generated carriers will be collected less in compared to a device with thinner or no PI layer.On the other hand, it is preferable to have a lower dark current to get a higher dynamic range and lower noise. Referring to figure 2.8 , it can be seen that the turn-off dark current for the samples with at least 1 μm PI layer is less than 10 pA under applied bias of 600 V.

Therefore, in order to optimize the PI layer there should be a trade off between the performance metrics of the device: photoconductivity ratio and dark current. We define

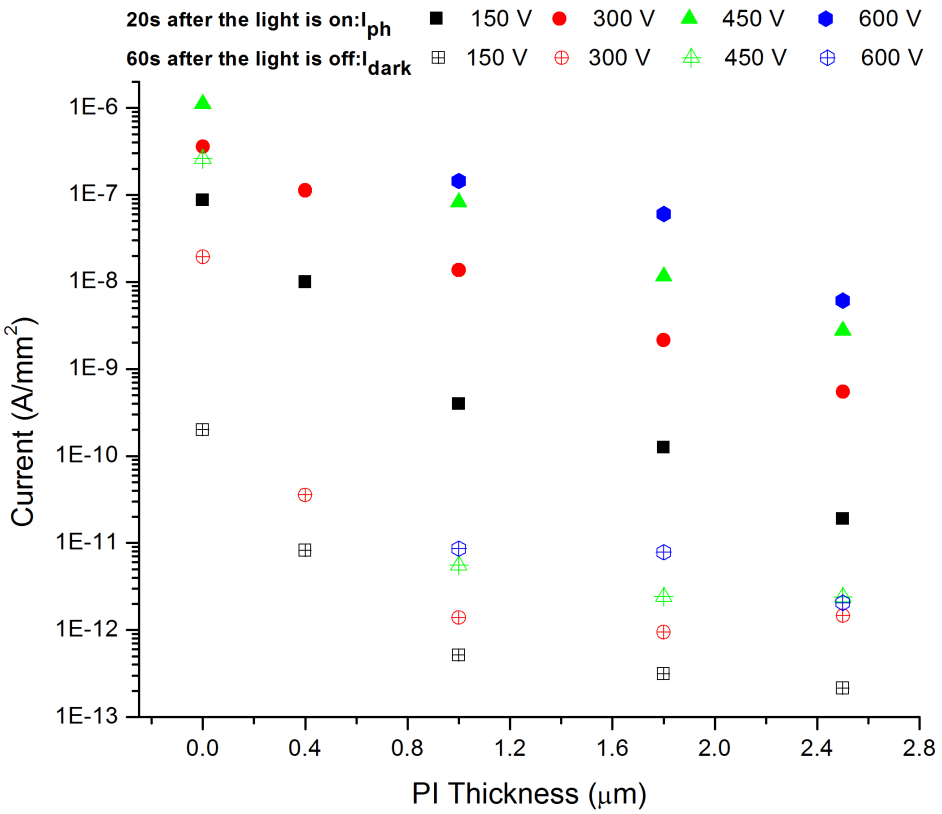

Figure 2.8: Photo and dark current of the samples under various electric filed. The turn-off dark current was measured 60 s after the light pulse (wavelength of 468 nm, with an intensity of 128 $\mu W/cm^2$) went off. And the photo current was measured in the middle of the illumination.

photoconductivity ratio as the photo current divided by the turn-off dark current at a specific electric filed. Figure 2.9 shows the photoconductivity ratio of the samples at various electric field. It can be seen that in sample S1, the amplitude of the dark current is getting closer to the photo current as we increase the voltage, so that the ratio of I_{ph}/I_{dark} is getting smaller. At $450V$ it has the smallest ratio in compared with the rest of the samples, which indicates that this device is not a good option for operating at high electric fields as it has a huge noise (dark current). At a very low applied voltage ($150V$), sample

S2, has the highest I_{ph}/I_{dark} ratio, since it has a thin PI layer, and thus under the same bias it conducts better in compared with the rest of the samples with PI layer. However, this changes by increasing the voltage to $300V$. Although the photocurrent of sample S2 is still higher than sample S3, but its dark current is increased more.

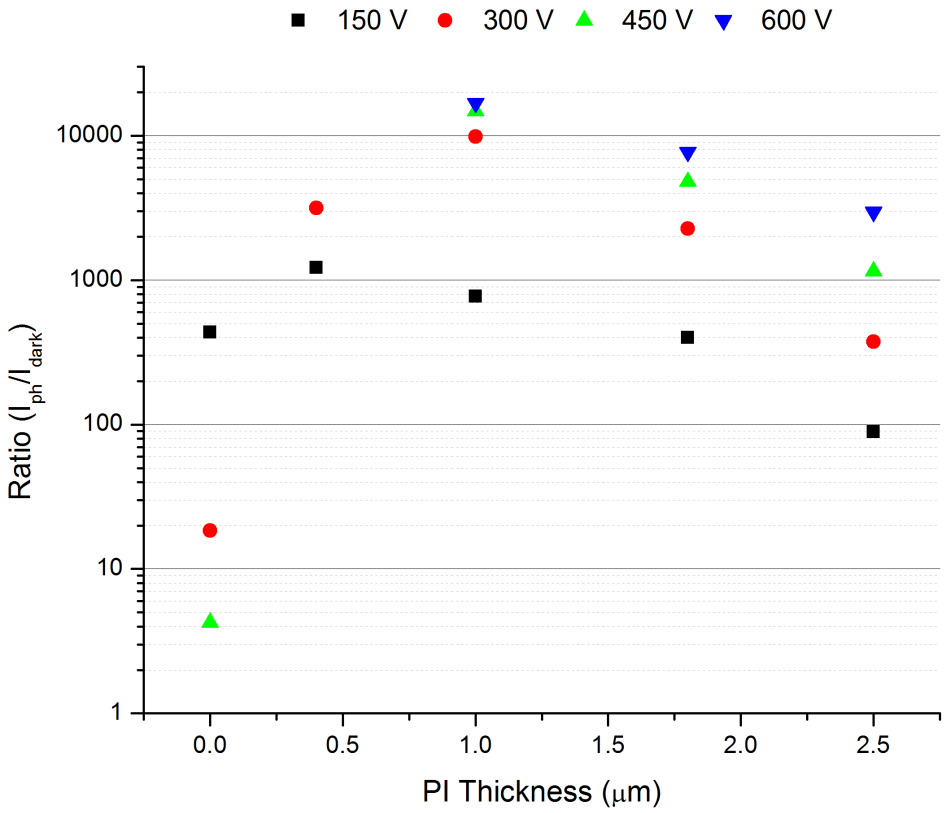

Figure 2.9: Ratio of Photo current to turn-off dark current (photoconductivity ratio) for the samples under various electric filed. The turn-off dark current was measured 60 s after the light pulse (wavelength of 468 nm, with an intensity of 128 $\mu W/cm^2$) went off. And the photo current was measured in the middle of the illumination.

From figure 2.9 it can be also observed that the ratio for thicker PI samples (S4 and S5) is increased by increasing the applied voltage, but they are still lower than S3. As an example sample S3 at $300V$ and S4 at $450V$ have the same photocurrent, however the

dark current in sample S3 is lower than sample S4. Therefore, too much increment of the PI thickness does not improve the device performance, since the thicker PI layer needs a higher electric field to conduct efficiently. Moreover, operating at very high voltages might be problematic in a packaging level, for instance it increases the possibility of sparking between the high voltage node and other parts of the package. These results suggest that sample S3 that has 1 μm PI layer has the best I_{ph}/I_{dark} ratio at higher electric fields which is a region of interest for operating the device.

From the results of these measurements, it was found that both dark current and photo current were decreasing by increasing the thickness of PI layer measured under the same applied bias. Comparing the photoconductivity ratio (I_{ph}/I_{dark}) suggests that sample S3 (1 μm-thick PI) has the best response at higher electric fields ($> 10V/\mu m$) which is a region of interest for operating the device. It was found that sample S3 is thick enough to keep the dark current as low as $10pA/mm^2$, and at the same time it is not too thick, so that the voltage drop across a-Se is sufficient to achieve a high photogeneration efficiency. Further, the PI layer uses a simple fabrication process that can be easily integrated into current large area digital imager manufacturing processes and it is a promising material for the development of high conversion gain a-Se detectors. However, this exact structure (metal/PI/a-Se/metal) has some limitations in terms of readout circuitry, such as active pixel sensor (APS). As discussed, in order to achieve a high conversion gain with low dark current, the bottom electrode which has a blocking layer should be positively biased in compared with the top electrode. Therefore, this structure would have difficulties while integrated with the hole collector APS circuit, since practically high voltage cannot be applied to the bottom electrode of the sensor as it is shared with the APS circuit. It should be also noted that PI as a blocking layer only can be coated prior to the a-Se deposition, otherwise a-Se would be crystallized due to the high temperature curing of

PI. Hence, in order to get the best performance out of the detector, instead of applying positive voltage to top, negative voltage can be applied to the top electrode. In this case, the sensor would work with only electron collecting APS circuit.

Chapter 3

Time of Flight Technique and Measurement

3.1 Introduction

Time of Flight (TOF) technique is a powerful tool which is widely used for the extraction of the charge carrier mobility in highly resistive, low mobility solids. This technique was first used by Spear in 1968. In this chapter the detailed principle of the TOF technique is described followed by the experimental setup and results. Using this technique we have investigated the voltage drop across PI film within the PI/a-Se stack.

3.2 Time of Flight Principles

The TOF experimental configuration is shown in figure 3.1. The material under the study (amorphous selenium) is sandwiched between two electrodes, one of which is transparent

(ITO coated glass), and also both electrodes should prevent re-injection of charge carriers into the bulk of a-Se. As it is shown in the figure 3.1, a voltage source is connected to the transparent electrode, and the other electrode is grounded through a resistor. This generates an uniform electric field within the device. As a short pulse of laser radiates towards the sample, electron hole pair (EHP) is created close to the interface of a-Se and PI. The absorption depth should be small compared to the thickness of the sample, which depends on the material and the wavelength of the excitation source. For a positively biased sample, holes drift toward the grounded electrode under the influence of uniform electric field and at a constant speed, and the transient photocurrent would be displayed on the oscilloscope. The hole mobility is defined as:

$$\mu_{hole} = \frac{L^2}{V t_T}, \tag{3.1}$$

where L is the material length, V is the applied voltage, and t_T is the measured transit time. It should be noted that by changing the polarity, instead of holes, electrons would travel through the bulk of a-Se and then the signal shown on the oscilloscope would be corresponded to the electron mobility.

The narrow sheet of charges drifts through the thickness of a sample at a constant speed and by assuming no carrier diffusion occurs, at the transit-time, the signal will fall to zero all of a sudden. In order for the oscope to be able to display the signal properly, the transit-time should be more than the product of load resistance and node capacitance (capacitance of device, cables, and any parasitic components). If the charge sheet reaches the collecting electrode cleanly, the charge transport is non-dispersive as it is shown in figure 3.2 a, and if a large number of carriers trap while transporting, due to the shallow trapped states, the charge transport is recognized as dispersive. In this case (dispersive) it takes longer

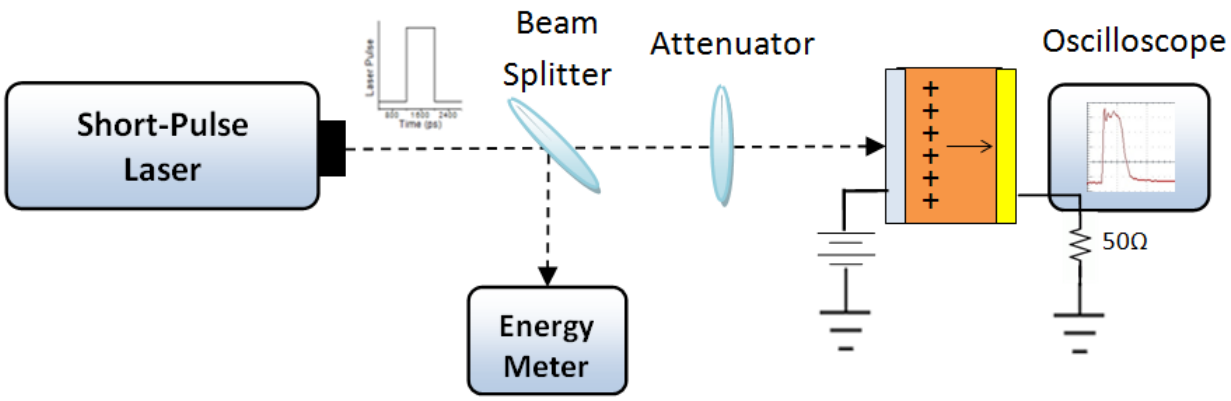

Figure 3.1: Typical time of flight setup.

for the charges to be de-trapped [8, 64]. The case between these two mechanism is called semi-non-dispersive charge transport which involves with a few number of trapped carrier within the charge drifting towards the collecting electrode. For a non-dispersive transport the transit time is defined either at t_0 or at the half magnitude point on the photocurrent tail (average transit time of carriers) as it is shown in figure 3.2 a. For dispersive case the transit time is calculated at the break in a log-log plot of the photocurrent vs. time or at the average time of the carriers' transit; which is shown in figure 3.2 b. Scher and Montroll have studied on a theoretical model to describe the dispersive transport behaviour [65].

There are some requirements that must be met for this technique to be accurate, which are described bellow:

- $t_T \ll \tau_d$, where t_T is the carrier transit time across the sample thickness and $\tau_d = \rho\epsilon$ is the dielectric relaxation time of the material. It should be considered that if the relaxation time of a material is too fast, the excess charges (narrow charge sheet) will be neutralized before they cross the sample, and the data will not be accurate

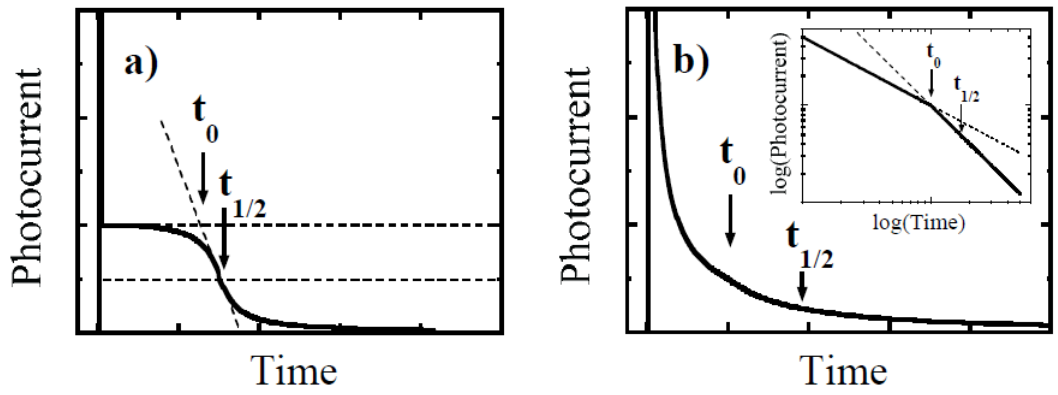

Figure 3.2: Time of flight signal for a non-dispersive and dispersive transport (adapted from [8]).

for the mobility measurement. The relaxation time for a high resistive amorphous semiconductors such as amorphous selenium and amorphous silicon are long enough that they can be studied by TOF technique.

- $t_{exc} \ll t_T$, where t_{exc} is the time it takes to generate the charge sheet. The light source should be sufficiently fast and generates short pulses that would be much shorter than the transit time. Otherwise, multiple charge sheets will be created while the carriers are drifting toward the electrode, and the photocurrent will not reflect the transient of a single sheet through the bulk of semiconductor. In this case it will be hard to calculate the accurate mobility.

- $\omega \ll L$, where ω is the charge sheet width, and L is the length of the sample. The charge sheet should be sufficiently narrow to drift toward the electrode across the sample. Further, the light source wavelength and intensity should be appropriate, so that the emitted light pulse is strongly absorbed by the material, and the penetration depth should be as thin as possible. For example amorphous selenium properties is

studied with xenon flash lamps and N_2 lasers [66]. Another factor that should be considered is that the amount of generated charges should be small enough so that it will not perturb the internal electric field. The internal electric field, $E = V/L$, is assumed to be uniform through the entire sample regardless of the position of the charge sheet. Otherwise, the transient response of the device will be different and the effect of the space charge on the electric field should be considered in the mobility calculation [67]. The duration of the high voltage power supply is also should be taken into account. The power supply should be applied for a short duration and only when the photocurrent is needed to be collected, this reduces the undesirable charge injection in to sample [61].

- Charge injection from the electrodes should be as small as possible to prevent charge build-up. The build-up charges will effect the electric field within the sample thickness, thus the photocurrent signal will be distorted. By increasing the applied voltage, this effect disturbs the photocurrent more severely. Therefore, contacts should be able to block the injection. As an example Johanson R.E. and co-workers investigated the effect of different metallic contacts on the injection of charges to a-Se bulk [36]. Alternatively, a blocking layers can be used between the material under study and the electrode in order to reduce the charge injection to the semiconductor. In this way TOF technique will be more accurate and can be performed for high electric fields.

- $R_{ext} < R_{sample}$, where R_{ext} is the external circuit resistor and R_{sample} is the resistor of the sample, so that the applied bias fully drops across the sample.

Equation 3.2 expresses the voltage across the external impedance in a Laplace transform:

$$V(s) = \frac{R}{sRC + 1} I_{ph}(s), \tag{3.2}$$

where $V(s)$ and $I_{ph}(s)$ are the Laplace transform of the output voltage and the photocurrent, R is the external resistance, and C is the combination of the sample, external, and the parasitic capacitance. Depending on the characteristics of the external circuit and the sample capacitance, the induce photocurrent can be collected in either current mode or voltage mode:

- **Current-mode:** if $RC \ll t_T$ the inverse Laplace transform yields to the following equation for the voltage. The collected charges go through the external resistor and the signal in figure 3.3 a would be shown on the oscilloscope, which is an ideal current-mode TOF signal.

$$v(t) = \begin{cases} Ri_{ph}(t) & 0 < t < t_T \\ 0 & t > t_T \end{cases}$$

- **Voltage-mode:** while $RC \gg t_T$, which leads to the following equation for the voltage across the node capacitor. The generated charges will build up over the node capacitor. Hence, an ideal voltage-mode TOF signal is shown in figure 3.3 b.

$$v(t) = \frac{1}{C} \int_0^t i_{ph}(t')dt'$$

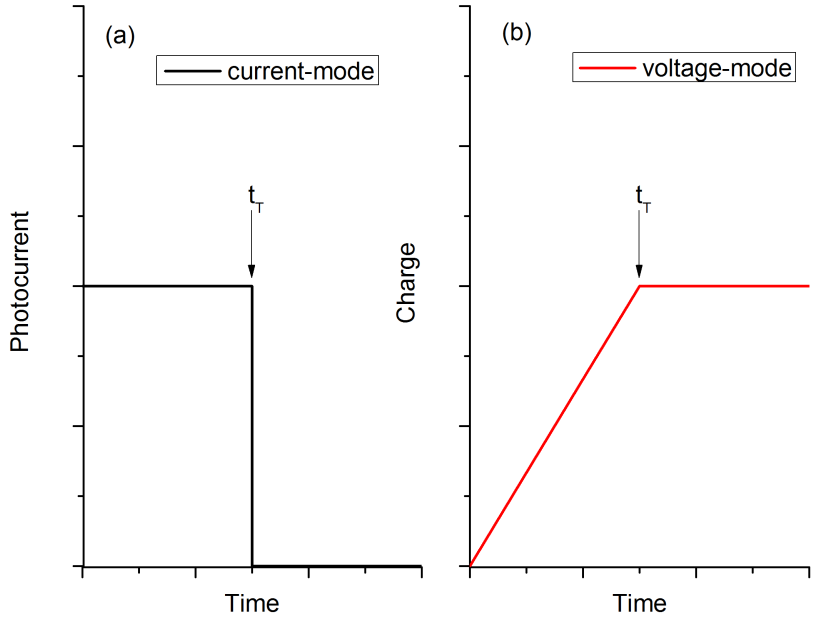

Figure 3.3: Different modes for TOF signal, (a) non-dispersive current-mode, (b) non-dispersive voltage-mode (adapted from [8]).

3.3 Sample Preparation

As it was discussed in the previous section, one of the requirement for the TOF experiment is that $t_T \ll \tau_d$. The relaxation time is define as $\tau_d = \rho\varepsilon$, where ρ is the resistivity, and ε is the dielectric constant of the material. If we do the calculation for a-Se with a resistivity and relative dielectric constant of 10^{14} $\Omega.cm$ and 6.7 respectively, the relaxation time is almost 60 seconds. Typically the transit time for a-Se film is in the range of micro or even nano seconds, so that this criteria has been met for a-Se. Further, there has been a study that demonstrated amorphous selenium charge transport falls in to a non-dispersive category, and the TOF signal will be looks like figure 3.3 [68].

As it is shown in figure 3.4 ,two samples were prepared: 16.5 μm thick a-S film with 1 μm

($S1$) and 1.8 μm ($S2$) polyimide as a blocking layer sandwiched between the transparent indium tin oxide (ITO), and the gold top contact. Wires were attached by using silver paste on the electrodes. It should be mentioned that the a-Se film was deposited in the same process run and all other conditions stayed the same except the polyimide thickness for these two samples.

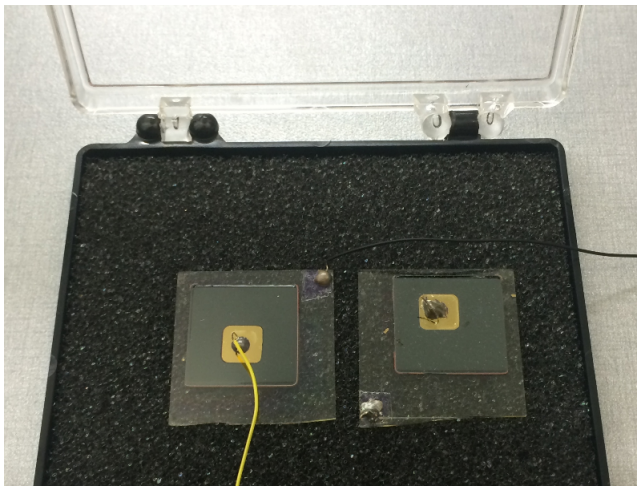

Figure 3.4: Amorphous selenium photodetectors with a poyilmide film as a blocking layer for time of flight measurement. The left sample has 1 μm-thick poyilmide film and the right one has 1.8 μm.

3.4 TOF Experimental System and Experimental Results

We have successfully set up the time of flight measurement system at the university of Waterloo in Giga-to-Nano lab. The components of the system is shown in figure 3.5. We used a N_2 laser (model # $GL-3300$) to produce a highly absorbed light for our a-Se-based

photodetectors. The laser generates a pulse in the range of 800 ps at the wavelength of 337.1 nm. The power supply is Stanford Research Systems PS350 high voltage power supply, which is able to produce $\pm 1000V$ at a very low ripple. In order to capture and display the TOF signal a $500MHz$, $5GS/s$ digital oscilloscope was used. The sync-out connector on the laser was used to trigger the scope to display the signal. In order to record the energy of the laser pulse, a beam splitter was used with a reflection/transmission ratio (R/T) of 50/50 to reflect 50 % of the laser beam to the energy meter. In order to prevent charge build-up and TOF signal distortion, a couple of neutral density filter was used to reduce the light intensity. The sample was placed on a sample holder, and in a low noise black box with an opening which was exactly aligned to the laser beam. The oscilloscope was functioning with a relatively low impedance (50 Ω). The high voltage was not controlled, however the measurement was performed as fast as possible to reduce the charge injection from the electrodes. Moreover, the polyimide layer helps blocking the hole injection from the positive bias of the electrode, so that we were able to get the TOF signal accurately.

3.4.1 Electric Field Calculation across Amorphous Selenium Film

In order to calculate the accurate electric field across the a-Se film, the conduction mechanism of polyimide was investigated by performing TOF measurement for two samples with different polyimide thicknesses. The polyimide thickness was varied by controlling the speed of the spin coating system. The time of flight results were compared to the high gain avalanche rushing amorphous photoconductor (HARP) sample. Harp sample has a thin blocking layer, so that they can assume that all the applied voltage will drop across a-Se film and simply find the electric field [69]. However, in our case the blocking layer thickness is around 1 μm blocking. As a result of this thick blocking layer, the electric

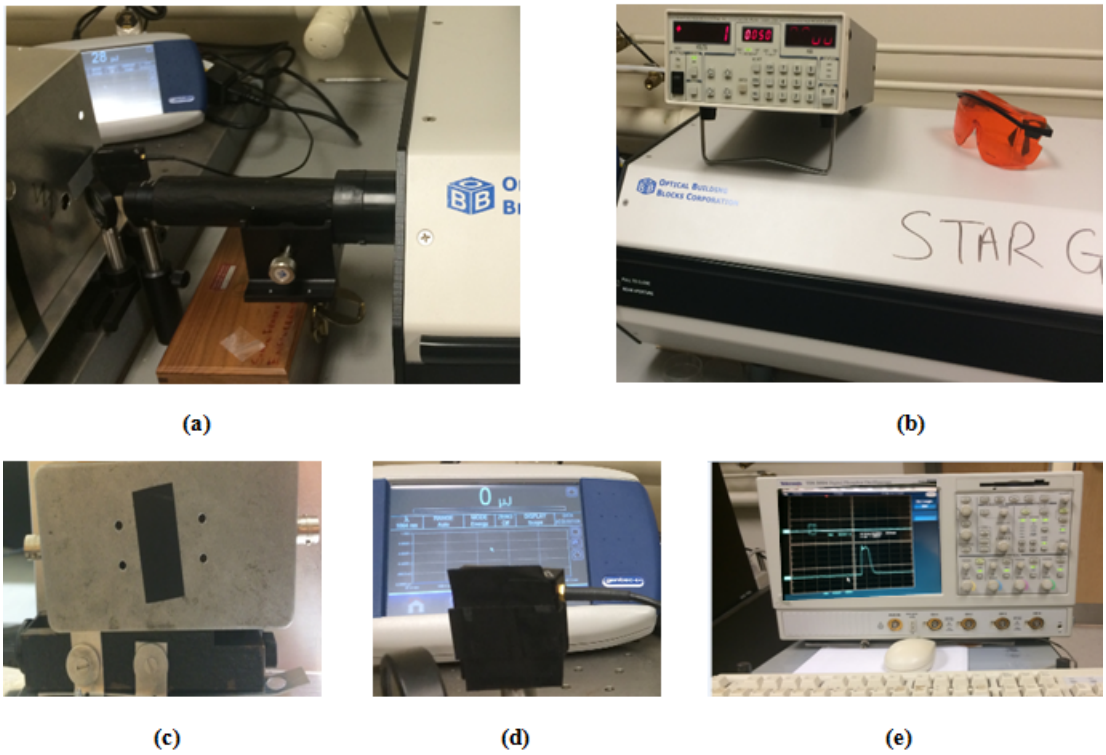

Figure 3.5: Time of flight experimental system. (a) optical components, nuetral density filter and the beam splitter alighned to the laser beam. Energy meter sensor is alighned to get the beam from the beam splitter. (b) High voltage power supply on the top, and the N_2 laser on the bottom. (c) low noise box with two BNC terminals to apply a high voltage and get the output signal. (d) Energy meter and the sensor. (e) Digital oscilloscope with an internal input resistance of 50 Ω.

field across amorphous selenium is unknown and we need more analysis to calculate it.

Polyimide acts as an insulator that blocks the hole injection from the positively biased electrode. Thus, we observe a very low dark current, i.e. for a device with 1μ m-thick polyimide layer and 16μ m-thick a-Se, the dark current was below 1 nA/mm^2 under 92 $V/\mu m$ [10]. On the other hand, when we illuminate the device with a specific wavelength, the conductivity of the a-Se increases, and the polyimide starts to show a different be-

haviour and it does not prevent the drift of photo generated carriers. In another study it was shown that the electric field across polyimide should be above a certain level ($1.4MV/cm$) to start conduction, due to Fowler-Nordheim type tunnelling injection of electrons [70].

It is valid to assume that under a steady state condition, a-Se and PI films act as resistors. So that electric field in a-Se can be calculated from a partial resistance of a-Se/PI structure. Table 3.1 shows the parameters needed to calculate the resistances of a-Se and PI films, as well as the calculated resistances value. However, we know that by increasing the applied voltage, the mobility of the a-Se increases. As a result of this, the conductivity of the a-Se film changes due to equation 3.3. Therefore, we need to find the electric field dependence of the a-Se film resistance to calculate the exact electric field in a-Se from the partial resistance of the sample structure.

$$\sigma_{hole} = e\mu_h P = e\mu_h \left(N_v e^{\frac{E_f - E_v}{KT}} \right), \tag{3.3}$$

where σ_{hole} is the hole conductivity, μ_h is the hole mobility,N_v is the defective density of states in the a-Se film, which is $10^{19} cm^{-3}$, $KT = 0.0256\ eV$,and $E_f - E_v = 1\ eV$.

Table 3.1: Resistance parameters for a-Se film and PI

Film	Resistivity (Ωcm)	Thickness (μm)	Area (mm^2)	Calculated Resistance (Ω)
a-Se	2.5E16 ($\mu_h : 0.1 cm^2/V.s$)	16.5	1	4.2E13
PI	1E17	1	1	1E13
PI	1E17	1.8	1	1.8E13

In order to verify whether the mentioned assumption is valid or not, we have conducted the TOF measurement on two different samples S1 and S2 which has $1\mu m$ and $1.8\mu m$ thick

PI respectively (both have 16.5μm a- Se). Figure 3.6 shows the TOF signal for the sample S1 and S2 at the 350V and 460V applied voltage respectively. Considering the measured resistances in table 3.1, the voltage drop across a-Se film and the calculated hole mobilities would be:

Sample #	Voltage drop across a-Se film (V)	Electric field across a-Se film ($V/\mu m$)	Mobility ($cm^2/V.s$)
S1	$0.8 \times 350 = 280$	17	0.08
S2	$0.7 \times 460 = 322$	19.5	0.07

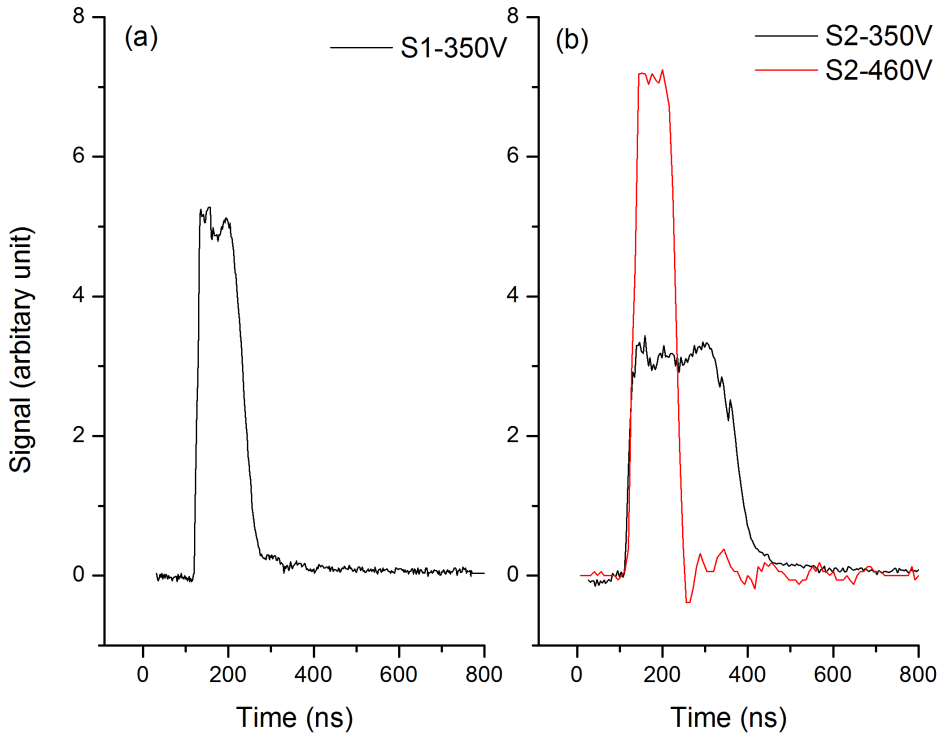

Figure 3.6: Time of flight signal for 16.5 μm-thick amorphous seleniuem film sandwiched between ITO and Au. Various thickness of polyimide was coated in between the a-Se and ITO as a hole blocking layer. (a) Device with a 1 μm-thick PI under 350 V applied voltage. (b) (a) Device with a 1.8 μm-thick PI under 350 V and 460 V applied voltage.

The values of the calculated mobilities are too low in compared to the previously reported mobility [71]. More importantly, as discussed before, the mobilities would increase by increasing the electric field, however, the calculated mobility based on the partial resistance voltage divider (in table 3.4.1) tends to decrease at higher electric field. Moreover, if we calculate the electric field across the polyimide film, the results for S1 and S2 would be 70 $V/\mu m$ and 77 $V/\mu m$ respectively. These values are so much lower than the sufficient electric field across polyimide layer to have an efficient conduction, i.e. (140 $V/\mu m$). All these factors considered, we can conclude that at least at low applied electric filed the voltage drop across a-Se film in the a-Se/PI structure should not be calculated by considering the resistances. We have to use other analysis to calculate the exact electric field across a-Se film to get the accurate mobility.

Therefore, in order to calculate the exact electric field within the a-Se, we have to consider the conduction mechanism in PI film. As it was mentioned before, two samples have been prepared with two different PI thickness (sample S1 and S2). Since the thickness and mobility of a-Se film for these two sample are exactly the same, at the same electric field, we should observe same transit time. As it can be seen in Figure 3.6 a, for the sample S1, the transit time of $120ns$ has been observed. Therefore, for sample S2, we applied different voltages (starting from 350V) to get the same transit time as sample S1 at 350V. As figure 3.6 b shows, at 460V applied bias on sample S2, $120ns$ transit time was observed. This means that by an increment of 0.8 μm polyimide layer, we had to increase the applied voltage by 110 V to get the same transit time. This yields to an electric filed of $110/0.8 = 137.5V/\mu m$ across the 0.8 μm polyimide layer which is consistent to our previous discussion. Based on this experimental results, the calculated electric field and hole mobility is shown in table 3.4.1:

Hence, we need to consider that the polyimide layer needs almost $138V/\mu m$ to have a

Sample #	Applied voltage (V)	Electric field across a-Se film ($V/\mu m$)	Mobility ($cm^2/V.s$)
S1	350	12.8	0.11
S2	350	6.2	0.10
S2	460	12.8	0.11

good conduction. This yields to 138 V and 248 V voltage drop on polyimide for sample S1 and S2 respectively. The calculated mobility is going to be 0.11 $cm^2/V.s$ under 12.8 $V/\mu m$ applied electric filed. This value compared with the previously reported mobility appears to be valid. A slight variation between this value and the previously reported results might be due to the different amorphous selenium purity, or different TOF system. Further the transit time was measured at the half magnitude point on the photocurrent tail. If we assume the faster transit time the mobility is going to be much more comparable to the previously reported results [63].

In order to improve the accuracy of the TOF signal, there are some factors that should be taken in to account:

- A high voltage controller to prevent the charge build-up on the sample.
- Thicker samples to meet the $RC \ll t_T$ requirement at the high electric fields. Our oscilloscope time constant is in a range of 1 ns, and since by increasing the voltage the transit time is getting smaller; in the range of few ns for our 16.5 μm thick a-Se photodetector, it requires more analysis to derive the exact transit time from the TOF measurement. However, a sample with a thicker a-Se film will resolve this issue since it increases the transit time.

Chapter 4

Turn-off Behaviour of PI/a-Se Based Photodetector

4.1 Introduction

Temporal performance (lag and ghosting) of the photodetector is a critical aspect in real time imaging modalities. Hence, in this chapter we have studied the nature of lag in the PI/a-Se structure, and proposed a model for turn-off dark current of the device. First a brief background regarding the effect of temperature and electric field on the components of the dark current will be discussed, followed by the theoretical model and fitting parameters, such as hole detrapping rate.

4.2 Background Theory

As it was discussed before, the dominant component of the dark current is the primary due to the charge (hole) injection from the electrodes. The dark current should be kept as small as possible to increase the dynamic range of the detector. Further, the temporal performance of the detector should be taken in to account to get an artifact free images. Temporal performance of the detectors depends on the detector properties and operating condition. It should be noted that the frame rate in real-time imaging application is about $30Hz$, which implies the importance of the temporal performance in real time imaging. There are two main factors that can effect the temporal performance of the detector including lag and incomplete charge transport [72]. In order to describe the time dependence of turn-off dark current variation, we have studied the dark current after illumination for our in house fabricated a-Se photodetectors under different applied electric fields and different temperatures.

Figure 4.1 demonstrates the typical equivalent circuit for the device under illumination, where the photocurrent is modelled as a current source. The detector capacitance depends on the thickness of the photoconductive layer (a-Se), thickness of polyimide the layer, their dielectric constant and contact area. Neglecting the fringing field and assuming the parallel plate geometry:

$$C = \varepsilon\varepsilon_0 A/d, \tag{4.1}$$

where A is the contact area, d is the a-Se (PI) thickness, ε_0 is the permittivity of vacuum, ε is the relative dielectric constant of a-Se (PI). The value of R_{a-Se} is bias dependent and is calculated from the conductivity equation by including the effect of increase in mobility

as a function of the bias:

$$\sigma = e\mu_h(N_v exp(-(E_f - E_V)/KT), \tag{4.2}$$

where the effective density of states in a-Se is $N_v = N_c = 10^{19}cm^3$, $kT = 0.0256eV$, and $0.1 \leq \mu_h \leq 1$. The value of R_{PI} is extracted by separate measurements of the electroded polymer layer with same thickness and contact area before [7].

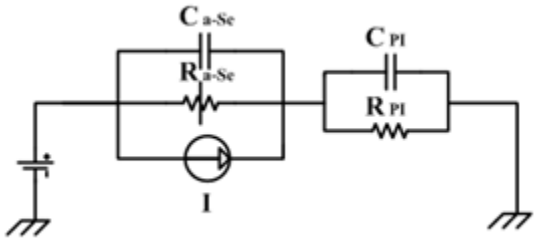

Figure 4.1: Demonstration of equivalent circuit for device under illumination.

Right after the applied voltage the dark current starts to decay to reach the steady state level. The transient response of the dark current after the applied bias is due to the depletion of holes from the defect states within the mobility gap, since the a-Se is slightly p-type [5, 47]. When the detector is exposed to the light source, the absorption depth is very small compared to the a-Se thickness, so that the generated electrons move quickly towards the radiation receiving electrode (bottom electrode) and holes drift in the a-Se bulk all the way to the top electrode. There are also generation of secondary EHPs by the impact ionization of holes at extremely high electric fields ($80V/\mu m$). A fraction of the generated carriers are going to be trapped in the a-Se bulk and interface defect states within the mobility gap during the irradiation. When the light source is turned off, the dark current decays to reach the steady state again. As it was discussed

before, the deep hole trap state exists $0.9eV$ above valence band and the deep electron trap state distribution is $1.2eV$ below the conduction band, which leads to a longer time for the trapped electrons (several hours) to be released in compared to the trapped holes (several minutes). Hence, in our model we have not considered the turn-off dark current corresponding to the detrapping of electrons. Considering these factors, the fitting will have three different components, including two exponential and one steady state terms:

- RC decay: $Ae^{(-t/\tau_1)}$, where A is the photocurrent right after the light source is turned off, and $\tau_1 = RC$ is the time constant of the detector.
- Hole detrapping: $Be^{(-t/\tau_2)}$, where $B \propto N_h \mu_h F$ is the detrapping coefficient for holes and τ_2 and is the average hole release time. Also N_h is the trapped hole concentration, μ_h is hole mobility and F is the electric field.
- Quasi-steady state dark current: D, which is related to the thermally generated dark current. The dark current due to the injection of carriers from the electrodes is negligible in this study because of the presence of hole blocking layer (polyimide) on the side of positively biased electrode (ITO) and gold as a top contact (cathode), which prevents the injection of electrons to the bulk of a-Se. It should be noted that the electron mobility is significantly lower than the electron mobility in a-Se bulk.

Employing these three components, the fitting of the turn-off dark current did not quite well matched with the experimental data. However, we were able to fit the dark current by using an extra exponential component as it is shown in figure 4.2. Hence, the turn-off dark current consists of at least three exponential and one steady state terms. The extra exponential term corresponds to the detrapping of the holes with higher time constant due to the existence of different interface defect states for holes in the a-Se bulk.

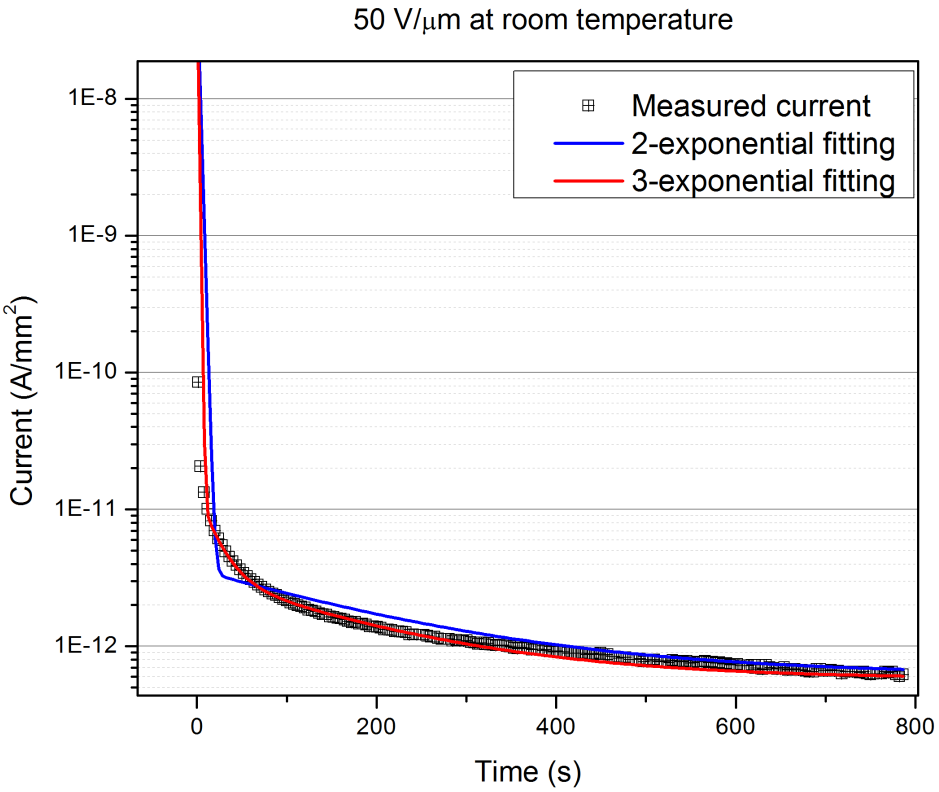

Figure 4.2: The 2-exponential and 3-exponential fitting for the dark current after illumination for an a-Se detector under $50V/\mu m$ electric field. The solide lines represent the fitted curves and the symbols represent the experimental data.

The turn-off dark current can be written as:

$$I_d = Ae^{(-t/\tau_1)} + Be^{(-t/\tau_2)} + Ce^{(-t/\tau_3)} + D, \tag{4.3}$$

In order to have a better understanding of the turn-off behaviour of the a-Se photodetector, we have conducted the experiments at different temperatures varying from 5 $^{\circ}C$ to 42 $^{\circ}C$. Therefore, the effect of temperature on different parameters of the modelled should be taken into account. Figure 4.3 shows the drift mobility as a function of the temperature,

which is controlled by the thermally activated tunnelling between states [9]. Haugen has been reported that the a-Se mobility will be saturated above room temperature. However, the mobility tends to be thermally activate below the room temperature, and it has been shown that the activation energy is $0.29eV$ which corresponds to the shallow trap depth [9].

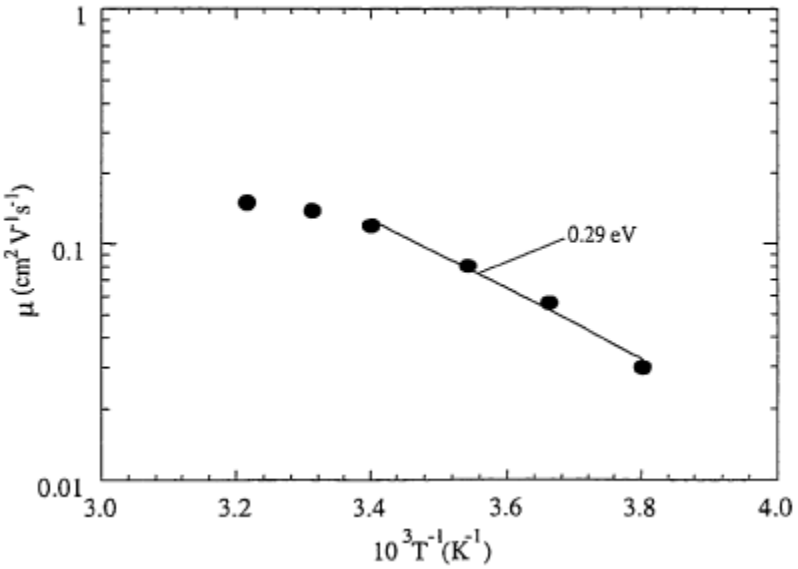

Figure 4.3: Hole mobility of the stablized a-Se as a function of temperature (adapted from [9]).

Another parameter that changes with temperature is the release time constant (τ_r) of the carrier, which is described as below for a discrete trapping level [51].

$$\frac{1}{\tau_r} = \upsilon exp(\frac{-E_T}{kT}), \tag{4.4}$$

where υ is a phonon frequency (typically $10^{12}s^{-1}$), k is the Boltzmann constant, T is the temperature of the material in Kelvin, and E_T is the energy depth of the charge traps. Therefore, the rate of the release charges is dependent with temperature. The rate of

releasing of the charge carriers is increased at higher temperature as the Boltzmann factor (kT) increases, leading to a lower release time constant.

The physical factors considered to find the fitting parameter are described below:

- $RC = \varepsilon\varepsilon_0/\sigma$ is the Maxwell relaxation time of the detector. Considering the PI/a-Se stack at room temperature the value of RC was calculated to be about $1s$ [7]. Increasing the temperature leads to the increment of the mobility, so that the RC constant decreases.

- The release time constant of holes in the a-Se bulk is in the range of $10s$ to $1000s$, and for electrons is several hours [73]. The barrier height for the traps in a-Se bulk does not change significantly with the applied electric field. For instance, at the applied electric field of $10V/\mu m$, the barrier height for the traps will decrease by $0.09eV$, and thus the average release time for holes and specially for electrons change slightly [61]. Therefore, in our fitting parameters the average release time was not changed significantly as a function of applied electric field. However, the release time decreased by increasing the temperature due to an increase of the Boltzmann factor (kT).

- The detrapping coefficient is related to the number of deep holes trapped in the bulk, which is increasing by increasing the applied electric field. The value of the mobility of our in-house fabricated a-Se photodetector as a function of electric field ($10V/\mu m$ to $50V/\mu m$) changes from $0.1cm^2/V.s$ to $0.45cm^2/V.s$ as it was previously reported [63]. Further, the mobility is temperature dependant and will increase by increment of the temperature.

- The time needed for the dark current to be reach the steady state is related to the average release time constant of the deeply trapped electrons and holes [61].

Therefore, the sample should be rested under applied bias and at dark condition for hours due to the long average release time for electrons. However, in this study we considered that the dark current reaches quasi-steady state after $1000s$.

4.3 Experimental and Theoretical Results

The structure of the prepared sample is shown in figure 4.4, where 16 μm-thick a-Se film and 2 μm-thick PI are sandwiched between the electrodes (Au and ITO glass). The coated polyimide on ITO acts as a hole blocking layer [7]. Further, the advantages of using Au as a top contact is that it acts as an electron blocking for the Au/a-Se junction [74]. The dark current and photocurrent of the device were studied at 22 $^{\circ}C$ (room temperature), 42 $^{\circ}C$, and 5 $^{\circ}C$ as a function of different applied voltages (ITO was positively biased). The applied electric field across a-Se layer varied from 10 $V/\mu m$ to 50 $V/\mu m$. As it was discussed before, the voltage drop across the polyimide differs in dark condition and light condition, due to the change of a-Se conductivity in the presence of photogenerated charge carriers. However, for simplicity of reporting the results for this study, since the PI layer thickness is the same ($2\mu m$) for all the measurements, the applied electric field values were derived based on the partial capacitances of the PI/a-Se structure. Figure 4.4 demonstrates the experimental setup that has been used for this study. A Stanford Research Systems PS350 high voltage power supply was used to bias the devices, and the current of the device was measured using an Agilent semiconductor parameter analyzer (4156C) and a low-noise probe station. In order to set the temperature, we used a Signatone S-1060R QuiTemp system with a hot chuck mounted inside the low noise box. The temperature of the substrate was monitored by using a thermocouple (Nickel-Chrome resistance wire) and the Omega digital panel meter for the whole duration of the experiment. The photoresponse of

the device was measured by illuminating a blue light ($468-nm$ wavelength) at an intensity of 100 $\mu W/cm^2$, with the pulse width and period of 20 s and 80 s respectively. The device was rested in between each measurement for at least twenty minutes in dark and under short circuit condition.

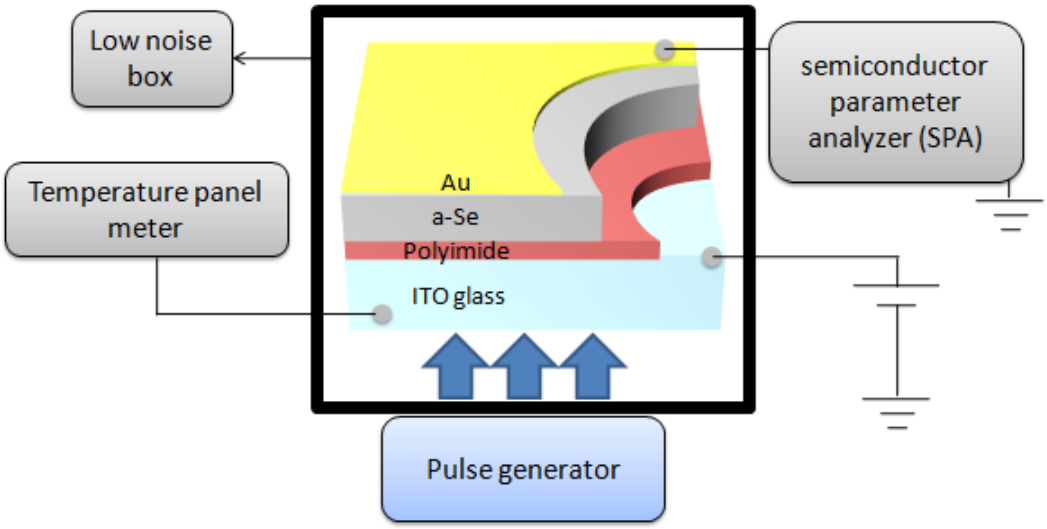

Figure 4.4: Setup and Device strcutes used of the experiment.

Figure 4.5 shows the photo and dark current of the sample at room temperature under different applied electric field. The dark current is decreased by two orders of magnitude after $1000s$ and it reaches to the quasi-steady state level. The device was illuminated to 5 pulses of blue light, and the dark current decays after illumination in about $900s$ to almost the value of dark current at the quasi-steady state before illumination. The dark current is increasing as a function of the applied electric field due to the more charge injection from the positively biased electrode.

Figure 4.6 represents the fitted model of the turn-off dark current for different applied

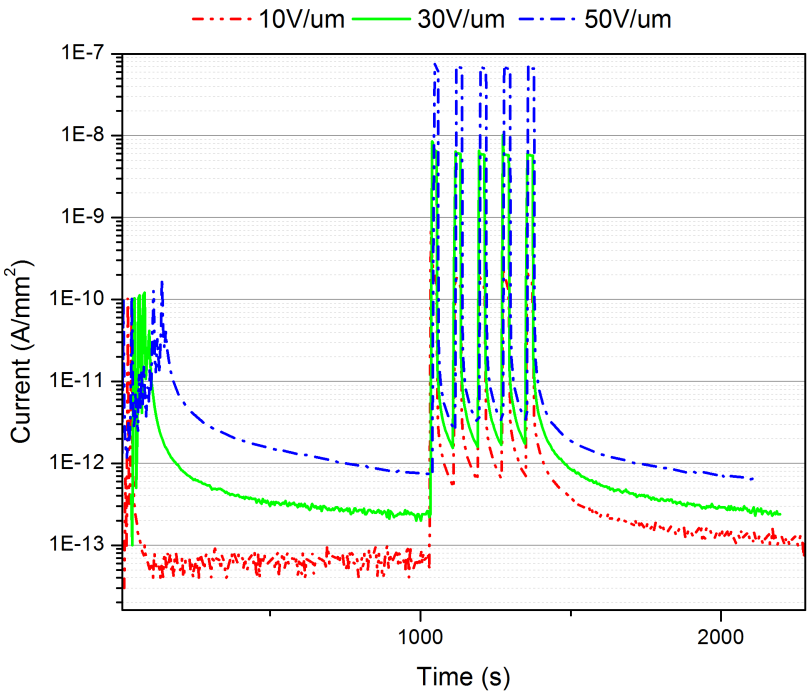

Figure 4.5: Photo and dark current of a-Se photodetector under various applied electric field. The device was rested for 1000s before illumination, and 900s after illumination, in which both dark currents almost reach to a quasi-steady state level.

electric fields at the room temperature, in which the turn off dark current is increasing by an increment of the applied electric field. The models were well fitted by using the parameters in table 4.1. The release time constant did not change significantly as a function of the applied electric field. Further, the detrapping coefficient increased as we increased the applied electric field. This can be related to the higher photocurrent, and higher trapped holes concentration at higher electric field.

Figure 4.7 represents the fitted model of turn off dark current at different temperatures under $10V/\mu m$ electric field. As it is shown in this figure, right after the light source is turned off, the dark current at $42°C$ decreases faster in compared to the room temperature,

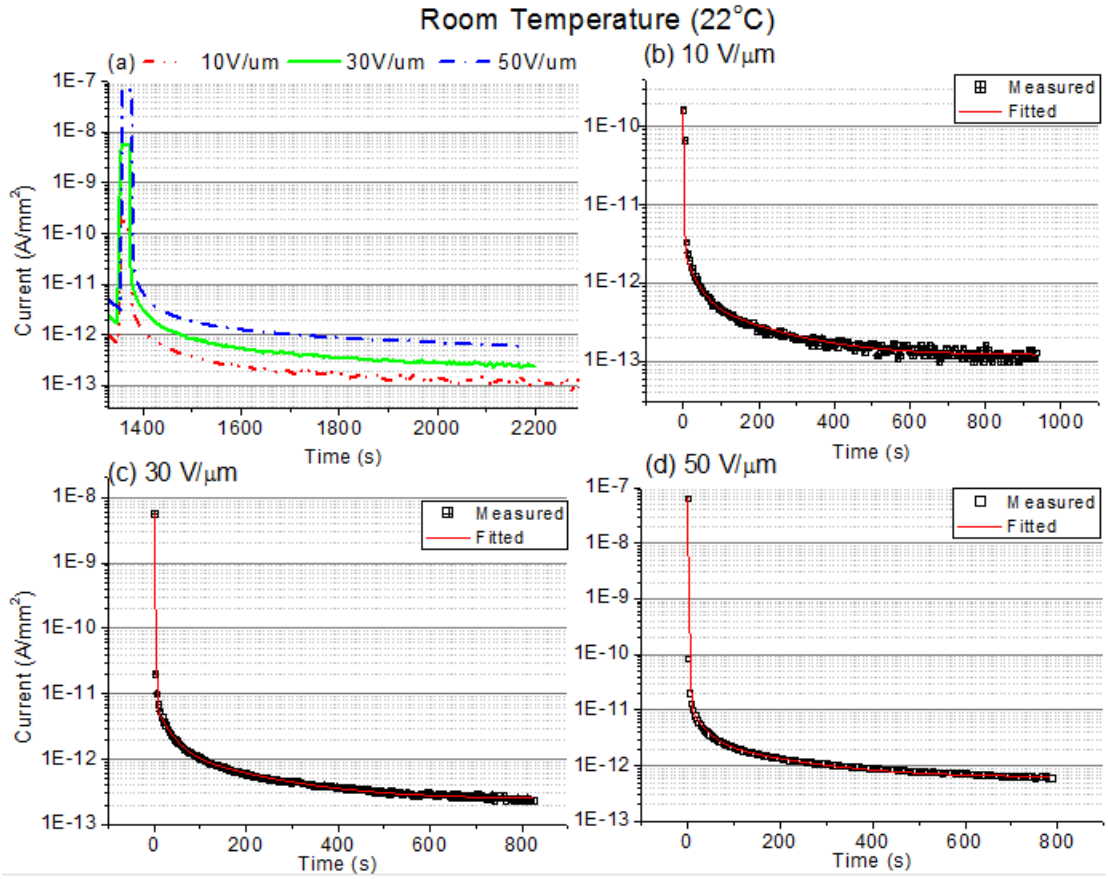

Figure 4.6: Expreimental and fitted model of the turn-off dark current of a-Se photodetector under various applied electric field at room temperature. (a) Measured photo and dark current at room temperature. Turn off dark current under applied electric filed of (b) $10V/\mu m$, (c) $30V/\mu m$, and (d) $50V/\mu m$, where the solide lines represent the fitted curves and the symbols represent the experimental data.

although its photocurrent was slightly higher than the room temperature. This is due to the lower RC and the detrapping time constant at $42°C$, so that the current decays faster. However, over the time more charges are going to be released at higher temperature which results in a higher dark current. At the quasi-steady state level, the dark current at $42°C$ is the highest due to the higher thermal dark current. The dark current at $5°C$ is the

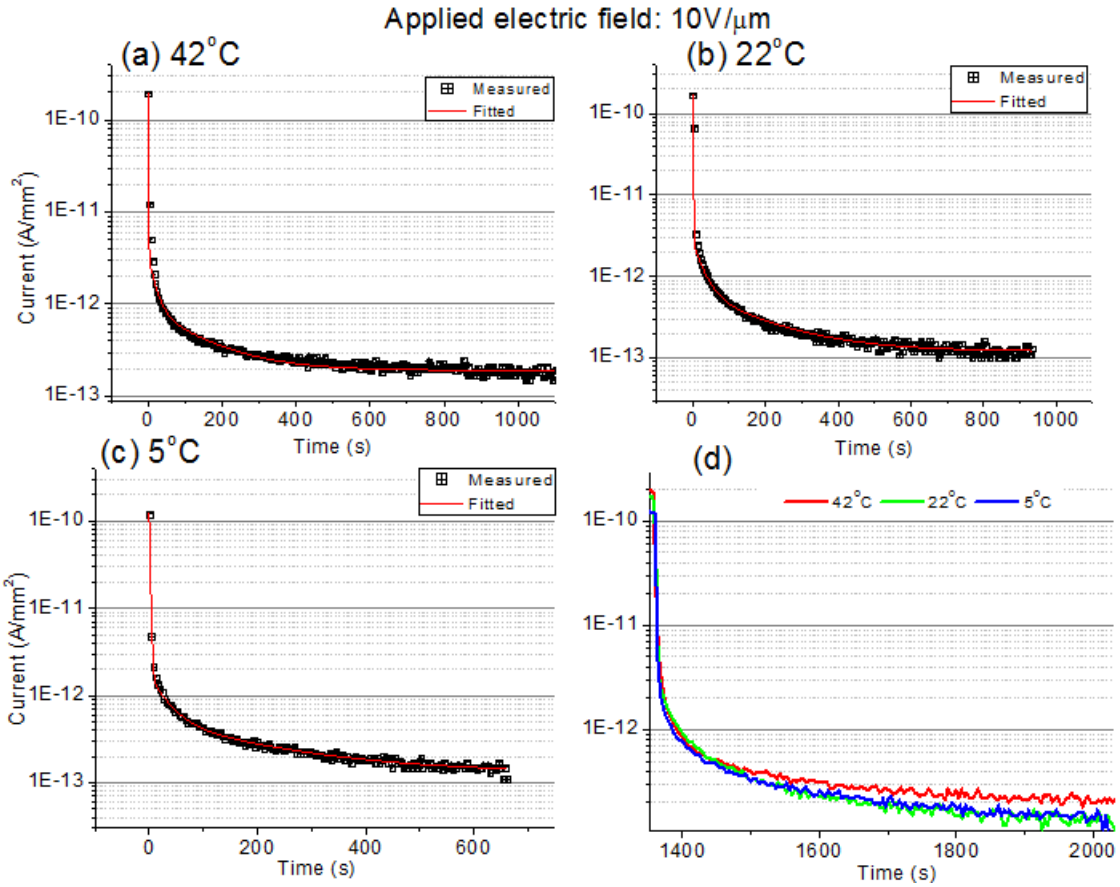

Figure 4.7: Expreimental and fitted model of turn-off dark current of PI/a-Se photodetector under $10V/\mu m$ electric fields at different temperatures. Turn off dark current at (a) $42°C$, (b) $22°C$, and (c) $5°C$, where the solide lines represent the fitted curves and the symbols represent the experimental data. (d) Measured photo and dark current at different temperatures.

lowest right after the illumination due to the lower photo current, lower mobility value and higher release time constant.

Further, at $5°C$ and $22°C$ the quasi-steady state dark current are almost the same, which is due to the higher release time of the trapped charges at lower temperature, and therefore it takes longer at $5°C$ that the trapped charges releases from the detector. If the sample rests

more, the dark current would reach the steady state, which is lower for $5°C$ in compared to higher temperatures. This is also shown in figure 4.8, in which before illumination the dark current at $5°C$ is the lowest due to the lower thermal generation dark current. The models were well fitted by using the parameters in table 4.1.

The experimental and fitted dark current is at higher electric fields is shown in figure 4.9 to 4.10, and the parameters used for fitting are shown in table 4.1.

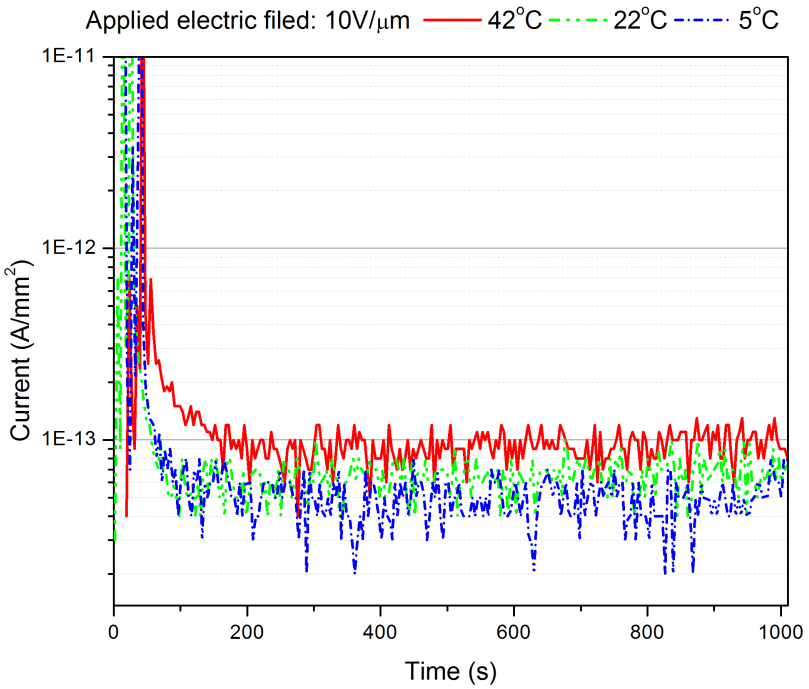

Figure 4.8: Dark current before illumination at different temperatures.

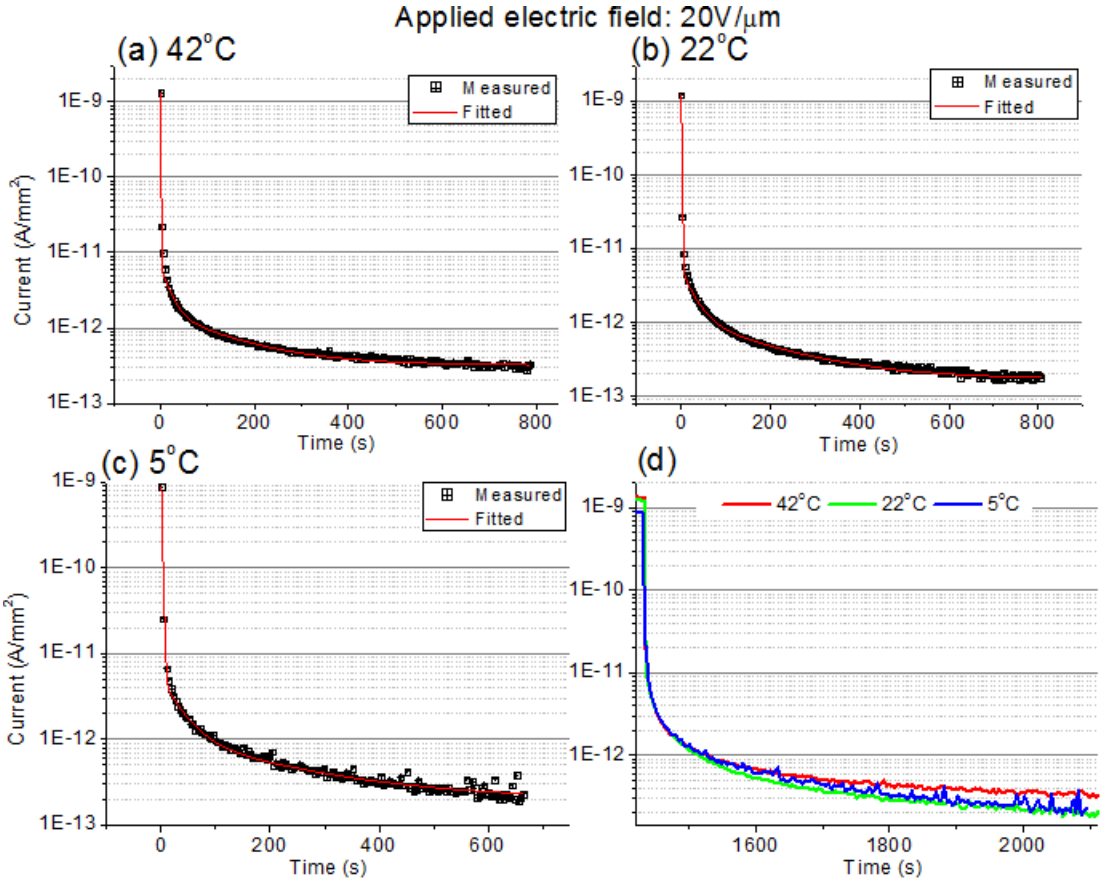

Figure 4.9: Expreimental and fitted model of turn-off dark current of PI/a-Se photodetector under $20V/\mu m$ electric field at different temperatures. Turn off dark current at (a) $42°C$, (b) $22°C$, and (c) $5°C$, where the solide lines represent the fitted curves and the symbols represent the experimental data. (d) Measured photo and dark current at different temperatures.

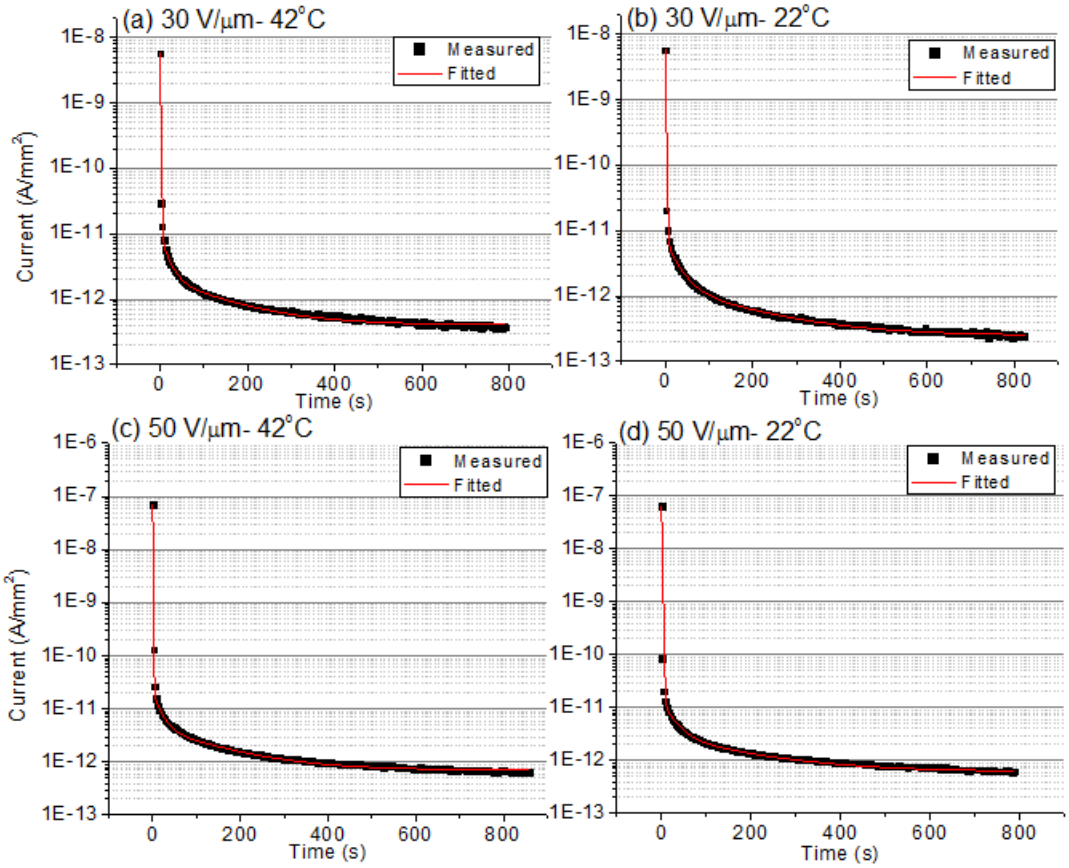

Figure 4.10: Expreimental and fitted model of turn-off dark current of PI/a-Se photodetector at $42°C$ and $22°C$ under $30V/\mu m$ (a and b), and $50V/\mu m$ (c and d) electric field.

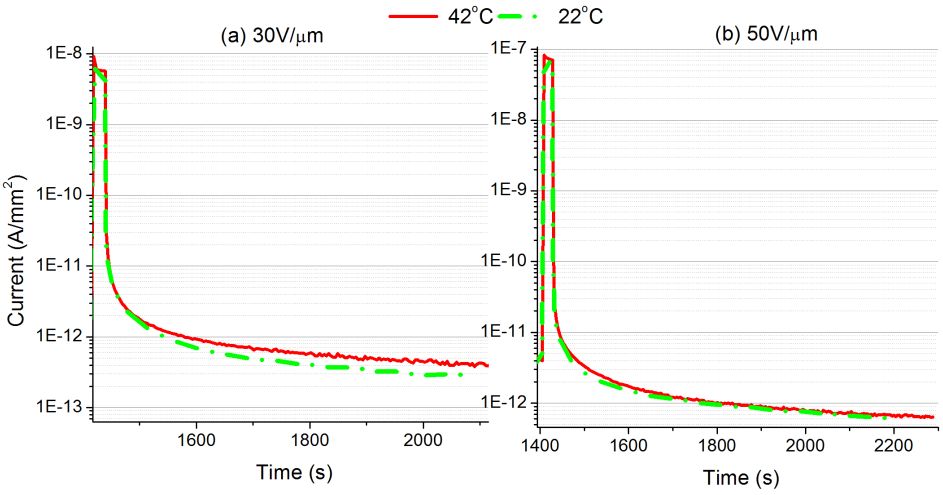

Figure 4.11: Expreimental turn-off dark current of PI/a-Se photodetector at $42°C$ and $22°C$ under $30V/\mu m$ (a), and $50V/\mu m$ (b) electric field.

The detrapping time constants are the material properties and depend on the fabrication processes. The photo and dark current response of the a-Se photodetector without blocking layer was measured to verify this. The experimental and fitted data are shown in figure 4.12, and the parameters used to fit the turn-off dark current are in table 4.2. The turn-off dark current is fitted with the same detrapping time constants, while the detrapping coefficients are higher by 4 orders of magnitude due to the large number of trapped holes in the a-Se bulk in case of not having blocking layer.

As it was discussed, under illumination the generated electrons move quickly towards the radiation-receiving electrode due to the small absorption depth compared to the a-Se thickness, and holes drift to the bottom electrode. Therefore, the transient behaviour of the dark current after illumination is due to the release of the bulk trapped holes. It should be noted that under extremely high applied electric fields, the secondary EHPs will be generated due to the holes impact ionization. In this case the electrons drift in the a-Se bulk towards the radiation-receiving electrode, so that the current related to the trapped electrons should be considered as well. The theoretical model and mathematical equation describing the lag response of the detector is still under more investigation.

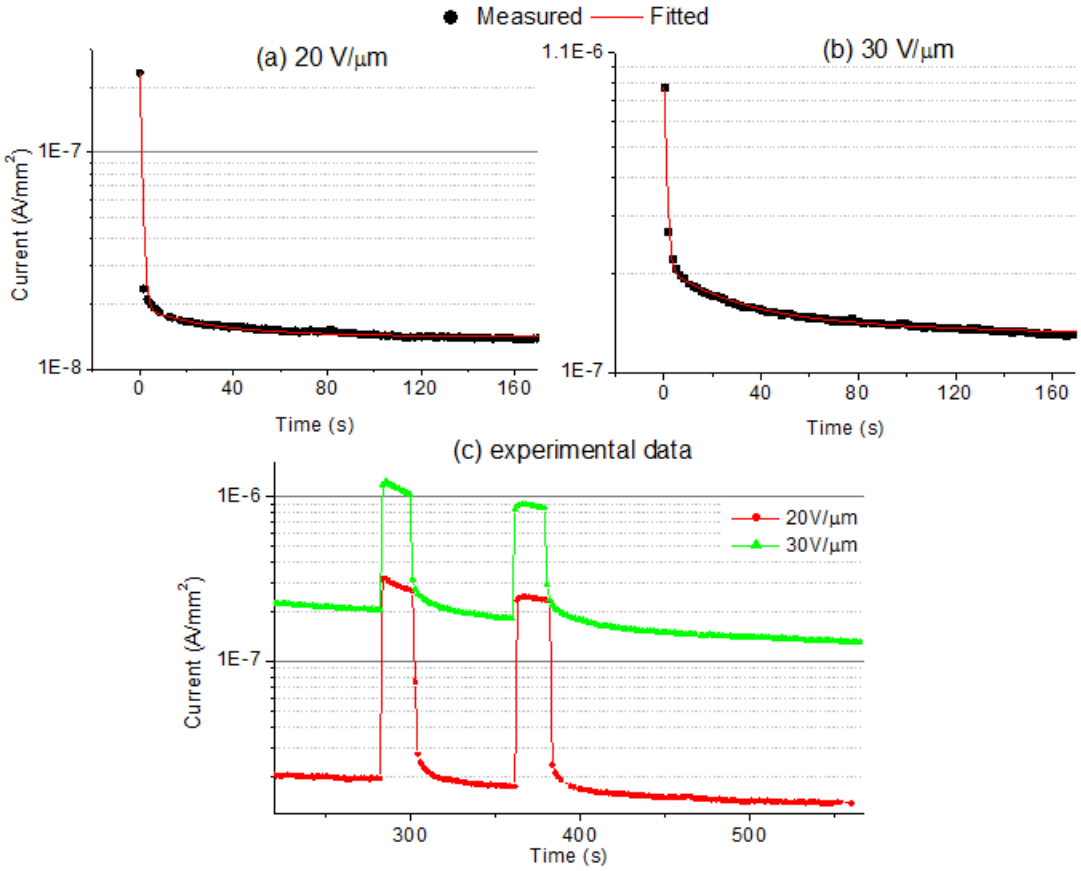

Figure 4.12: Expreimental and fitted model of turn-off dark current of a-Se photodetector without blocking layer at room temperature under $20V/\mu m$ (a), and $30V/\mu m$ (b) electric field. (c) Represents the measured photo and dark current under 20 and $30V/\mu m$ electric fields and at room temperature.

$$I_d = Ae^{(-t/\tau_1)} + Be^{(-t/\tau_2)} + Ce^{(-t/\tau_3)} + D, \tag{4.5}$$

$$A = Iph \ , \ B = eN_h\mu_h F \ , \ C = eN_{h2}\mu_h F \ , \text{ and } D = I_{off-steadystate}.$$

Table 4.1: The fitting parameters used for modelling the turn-off dark current of the PI/a-Se photodetector at different applied electric fields and temperatures (equation 4.5).

E-field ($V/\mu m$)	Temp (^oC)	τ_1 (s)	τ_2 (s)	τ_3 (s)	A (A/mm^2)	B (A/mm^2)	C (A/mm^2)	D (A/mm^2)
10	42	0.5	18	135	1.94×10^{-10}	2.5×10^{-12}	7×10^{-13}	1.9×10^{-13}
	22	1	26	170	1.67×10^{-10}	2×10^{-12}	5.4×10^{-13}	1.2×10^{-13}
	5	1.5	30	200	1.2×10^{-10}	1.2×10^{-12}	4×10^{-13}	1.3×10^{-13}
20	42	0.5	18	135	1.33×10^{-9}	5×10^{-12}	1.3×10^{-12}	3.2×10^{-13}
	22	1	26	170	1.22×10^{-9}	4×10^{-12}	1×10^{-12}	1.7×10^{-13}
	5	1.5	30	200	8.78×10^{-10}	4×10^{-12}	9×10^{-13}	2×10^{-13}
30	42	0.5	17	135	5.7×10^{-9}	7.5×10^{-12}	1.75×10^{-12}	4×10^{-13}
	22	1	26	170	5.7×10^{-9}	5.5×10^{-12}	1.2×10^{-12}	2.45×10^{-13}
40	42	0.5	16.5	135	2.26×10^{-8}	1×10^{-11}	2.5×10^{-12}	5×10^{-13}
	22	1	26	170	2.45×10^{-8}	7.3×10^{-12}	1.2×10^{-12}	4.7×10^{-13}
50	42	0.5	16	135	7.06×10^{-8}	1.5×10^{-11}	3.8×10^{-12}	7.2×10^{-13}
	22	1	25	170	6.8×10^{-8}	1×10^{-11}	2.4×10^{-12}	6.1×10^{-13}

Therefore, it can be concluded that lag behaviour that we observe in amorphous selenium based photodetector is inherent to the a-Se properties and the density of the trapped state. Further based on our model, the turn-off dark current is related to hole trapping rather than electron trapping in bulk of a-Se. Hence, the dark current variation after illumination is determined by holes releasing time constant in a-Se bulk (which is in the range

Table 4.2: The fitting parameters used for modelling the turn-off dark current of the a-Se photodetector under different electric fields and at room temperature (equation 4.5).

E-field ($V/\mu m$)	Temp (^oC)	τ_1 (s)	τ_2 (s)	τ_3 (s)	A (A/mm^2)	B (A/mm^2)	C (A/mm^2)	D (A/mm^2)
20	22	0.86	26	170	2.15×10^{-7}	5×10^{-9}	1.2×10^{-9}	1.36×10^{-8}
30	22	0.86	26	170	6.5×10^{-7}	6.6×10^{-8}	2.5×10^{-8}	1.28×10^{-7}

of 10 - 1000 sec). As it was discussed, due to the existence of different interface defect states for holes in bulk of a-Se and interface of a-Se and PI, we consider two detrapping time constants for holes. According to our fitted model to experimental results, hole detrapping time constant has been found 26 and 170 sec at room temperature and the number of trap density has been calculated $1.25 \times 10^{11}/m^3$ and $3.4 \times 10^{10}/m^3$. Moreover, as we expected, the detrapping time constant has not shown any variation as a function of electric field.

Chapter 5

Temperature Stability and Durability of PI/a-Se Photodetector

5.1 Introduction

An electrical device may be subjected to the environmental stresses during the transportation and storage, which can affect its performance. Stability is a very important requirement for a photodetector, which depends critically on the selection and design of the photoconductive layer. Qualification testing procedure is needed to test the photodetector with the accelerated stresses to check the margins of functionality. The main objective of this chapter is to show how well the PI/a-Se photodetector can handle the real transportation and maintenance condition.

5.2 Background Theory

For a medical device failure is not an option, therefore, it should be designed to operate as specified, and should not deteriorate over a long period of time or as a consequence of environmental or other stresses. Amorphous selenium has found its way in digital x-ray detectors for clinical radiology applications. One of the common problem of an a-Se film is gradually crystallization at room temperature due to its low glass transition point [75]. This phenomena would be expedited when the a-Se detector exposes to the higher temperatures. There have been some efforts to resolve this problem such as introducing various polymers as a protective layer [76, 77]. The crystallization growth rate is described in equation 5.1 which is highly temperature dependent [73].

$$R = R_{\circ} exp(\frac{-E_A}{KT}), \tag{5.1}$$

where $R_{\circ}$ is a constant, E_A is an activation energy, K is the Boltzmann constant and T is the absolute temperature. Crystallization of a-Se films results in the degradation of the device in term of increasing the dark current and image lag. As a consequence of increased dark current, crystallization of the a-Se film is accelerated due to the Joule heating. A high dark current reduces the dynamic range of the device and limits the lowest detectable signal. The operational lifetime of amorphous selenium at different temperatures was investigated previously. It was shown that at $40°C$ and $50°C$, the operational lifetime of selenium is 70 years and 10 years respectively [76]. They have also shown that the dark current was susceptible to the temperature change.

In order to improve the temperature resistance of the a-Se film, various polymers as a protective layer were introduced, such as fullerene (C60)-doped polymer [78]. The protective layer should have appropriate electrical, mechanical, and chemical properties to

improve the reliability of the device. It was also demonstrated that using a buffer layer promotes the photo-induced crystallization in a-Se film [79]. Some of the desirable requirements pertinent to the reliability improvement are listed bellow [80]

- Good adhesion to the substrates
- High Reliability
- Thermal Stability
- Low stress
- Minimal moisture uptake

In our photodetector structure we use a low-stress and low-moisture uptake polymer, polyimide(PI), to prevent the a-Se crystallization and increase the stability of the a-Se film. Further, the PI layer stabilized the a-Se film against photo-induced crystallization for $T = 280 - 345K$ [7]. In the next section, the stability of a-Se film with PI buffer layer has been demonstrated at different storage temperatures for various periods of time.

5.3 Experimental Results

5.3.1 Temperature Stability

We evaluated the stability of our a-Se-based photodetector with a hole blocking layer (PI) after being stored at different temperatures, below and above the glass transition (T_g) of a-Se ($\sim$40°C), for various duration. Table 5.1 summarizes the test specifications. The structure of the device consists of an 16μm-thick a-Se film with a 1μm-thick PI film as

a hole blocking layer. The detector was rested for 3 hours at room temperature before performing the measurement.

Table 5.1: Temperature Stability Test Specification

Test #	Temperature (°C)	Duration (h)	NO. Cycles	Resting Time Between Cycles(h)
1	30	3	1	-
2	45	5	1	-
3	55	3	1	-
4	45	2	3	2

The electrical behaviour of the detector is demonstrated for all the test conditions and under different applied bias in figure 5.1. The detector was rested under applied voltage for about $400sec$ at dark condition. The photocurrent of the device was measured with three pulses of $468nm$ wavelength light source at an intensity of $100\mu W/cm^2$ with a width and period of 20 and $80s$ respectively. The dark and photocurrent of the device at 20°C is considered as a reference. The experimental results of dark and photocurrent measurements shows no significant degradation in the photocurrent performance while the device has been exposed to high temperature for a specific time periods.

In order to get a better insight regarding the impact of temperature on the detector performance, the sensitivity of the device under different conditions, normalized to the reference sensitivity, was calculated, which is shown in figure 5.2. The sensitivity is defined in equation 5.2.

$$S = \frac{I_{ph}}{I_{dark}}, \tag{5.2}$$

where I_{dark} is a dark current right before the second pulse ($60s$ after the light was turned off) and I_{ph} is the photocurrent in the middle of the first pulse ($10s$ after the light was

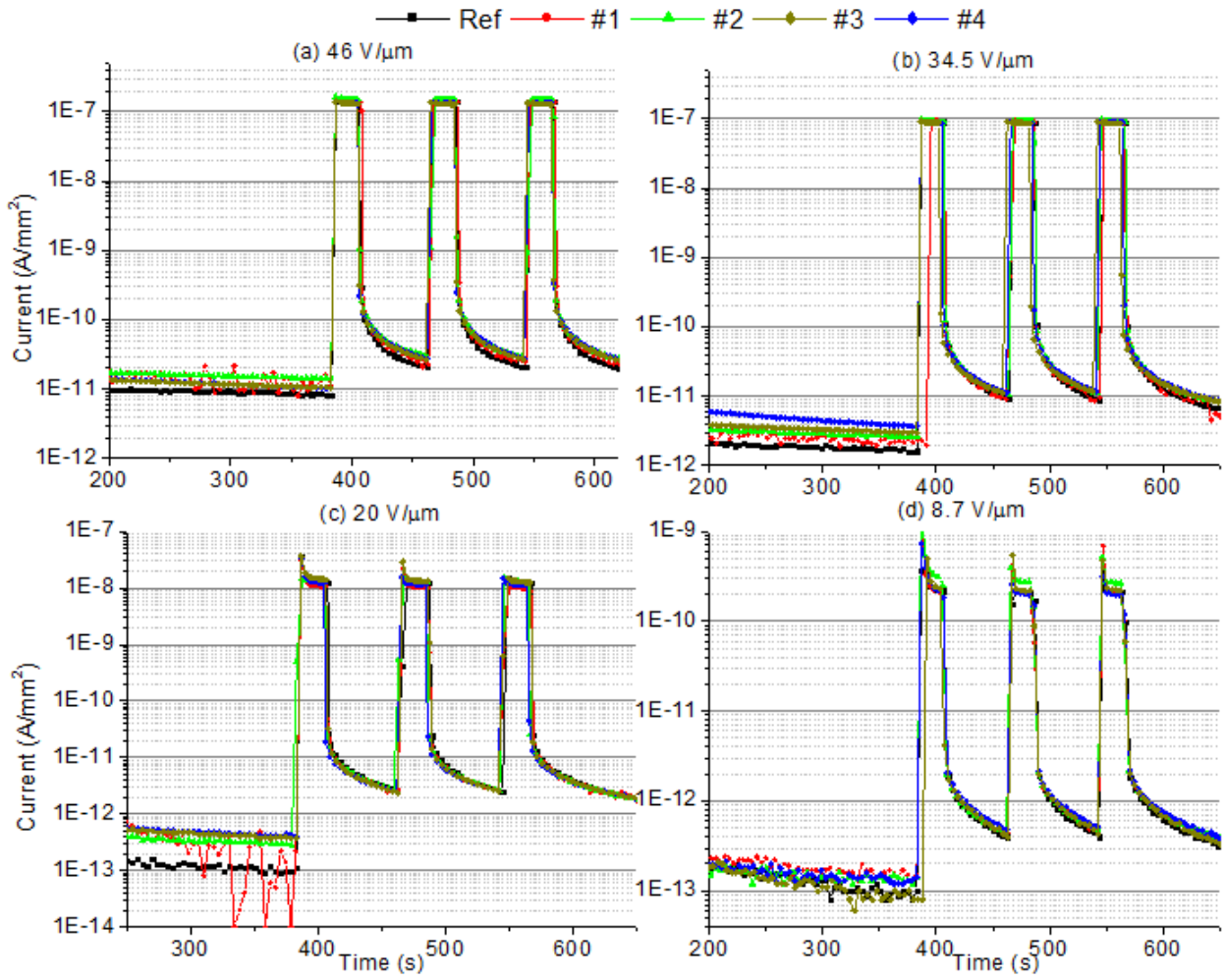

Figure 5.1: Accelerated heating impact on the dark current and photocurrent of the detector. The device was rested for 3 hours before performing the measurement; blue light with intensity of $100\mu W/cm^2$ was used and the device was rested for $400s$ under dark condition with an applied bias.The Applied electric field is: (a) $46V/\mu m$, (b) $34.5V/\mu m$, (c) $20V/\mu m$, and (d) $8.7V/\mu m$.

turned on). It can be seen in figure 5.2 that the normalized sensitivity of the photodetector does not change significantly at low electric field. However at higher electric field a small degradation of the normalized sensitivity is observed. This may be related to the creation

of deep traps in a-Se film by accelerated heating. The device should be restored fully if it rests longer at room temperature. Further, the case that the sample was exposed to 3 cycles of $45°C$ shows more degradation, since the resting time of the device was the same for all the tests. Thus, longer high-temperature exposure creates more trap density and needs more resting time to recover.

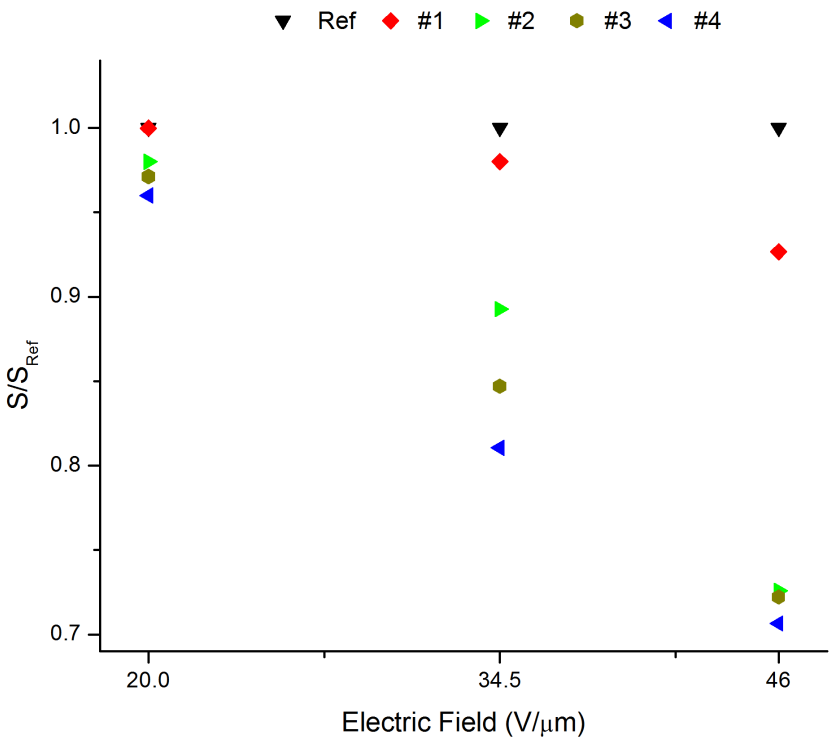

Figure 5.2: Photodetector sensitivity at different electric field after being stored at below and above glass transition point of a-Se.

5.3.2 Durability

We evaluated the stability of our a-Se-based photodetector as a consequence of several exposures to energy sources over time. The initial measurements were performed more than one year ago, and the recent tested electrical behaviour, dark current and photocurrent, in compared with the previous measurements shows no significant change [10]. All the conditions during the measurement were the same, and the same light intensity was used. The previously and recently measured dark and photo current of the same detector are demonstrated in figures 5.3 and 5.4 respectively. Conventional detectors had the problem of image lag due to the crystallization over the time. However, our detector does not show any deterioration in the electrical properties in terms of dark current and image lag compared to the previously reported results.

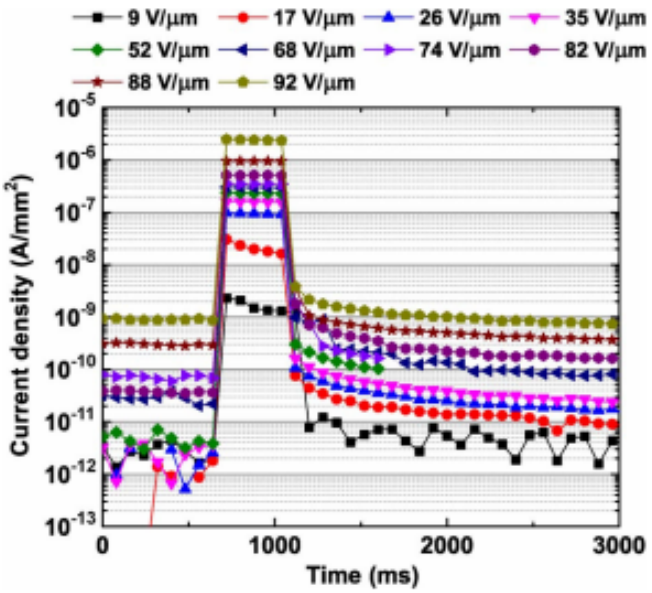

Figure 5.3: Previosuly reported dark and photocurrent of the a-Se-based photodetector with a blocking layer as different electric fields [10].

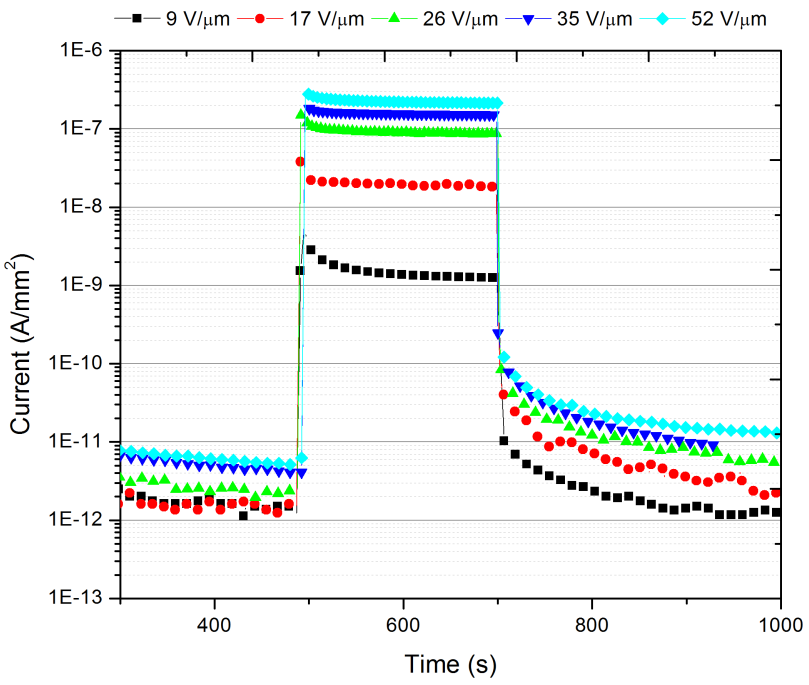

Figure 5.4: Recently measured dark and photocurrent of an 1-year old a-Se-based photodetector with a blocking layer at differnet electric fields.

Chapter 6

Conclusion

This work has investigated different aspects of the a-Se based photodetector with polyimide as a hole blocking layer. In order to achieve the most efficient device within the PI/a-Se structure, the dark and photo responses of different thicknesses of PI (varied from $0.4\mu m$ to $2.5\mu m$) have been studied. From the results of these measurements, it was found that both dark current and photo current were decreasing by increasing the thickness of PI layer measured under the same applied bias. Comparing the photoconductivity ratio (I_{ph}/I_{dark}) suggests that sample with 1 μm PI has the best response at higher electric fields ($> 10V/\mu m$), which is a region of interest for operating the device. It was found that 1 μm PI is thick enough to keep the dark current in the acceptable range for medical imaging applications (as low as $10pA/mm^2$), and at the same time it is not too thick, so that the voltage drop across a-Se is sufficient to achieve a high photogeneration efficiency. As discussed in Chapter 2, although this exact structure (metal/PI/a-Se/metal) has a good performance in terms of sensitivity and the ability of being operated in avalanche mode, it can be only integrated with the electron collecting APS circuit.

Further, the accurate electric field across the a-Se film has not been quite known within the PI/a-Se structure. This is important since the mobility of the charge carriers and the photogeneration efficiency, are strongly dependent to the electric field across the a-Se film. The photogeneration efficiency of the device is also related to the conduction mechanism of polyimide layer under various electric fields. Time of flight measurement has been carried out on different thicknesses of PI to find the exact voltage drop over a-Se film. Based on the TOf measurement, we have concluded that the polyimide layer needs almost $138 V/\mu m$ to provide a good conduction. Moreover, the hole mobility of 0.11 $cm^2/V.s$ under 12.8 $V/\mu m$ applied electric filed for a-Se has been calculated, which is in consistence with the previously reported results. A slight variation might be due to the different a-Se purity or different TOF measurement system.

Another aspect of the detector is the temporal performance (lag and ghosting), which is critical in high frame rate imaging application. In order to have a better insight of lag behaviour of the PI/a-Se photodetector, the dark current after illumination (turn-off dark current) at different temperatures and under various applied voltages has been studied. The results from these measurements are in agreed to the model that we propose for the turn-off dark current of PI/a-Se structure. Based on the results and the theoretical model, the lag behaviour in amorphous selenium based photodetector is inherent to the a-Se properties and the density of the trapped state. According to our model, it has been concluded that the turn-off dark current is due to the hole trapping rather than electron trapping in a-Se bulk. Hence, the dark current variation after illumination is determined by holes releasing time constant in bulk of a-Se (which is in the range of 10 - 1000 sec). Due to the existence of different interface defect states for holes in bulk of a-Se and interface of a-Se and PI, we consider two detrapping time constant. According to our fitted model to experimental results, hole detrapping time constant has been found 26 and 170 sec at

room temperature and the number of trap density has been calculated as $1.25 \times 10^{11}/m^3$ and $3.4 \times 10^{10}/m^3$ at $10V/\mu$ electric field. Moreover, as we expected, the detrapping time constant has not shown any variation as a function of electric field.

As discussed an a-Se film can gradually crystallize at room temperature due to its low glass transition point which can be expedited, it is being exposed to the higher temperatures. In our photodetector structure we use a low-stress and low-moisture uptake polymer, polyimide(PI), to prevent the a-Se crystallization and increase the stability of the a-Se film. Therefore, the temperature stability of the photodetector has been investigated, to see how well this device can handle the environmental stresses (high temperature) during its transportation and storage. Further, the durability of the device as a consequence of repeated light exposures over a year is studied by comparing its previous and recent dark and photo responses. From the results of these two measurements no significant degradation has been observed within the performance of the device, which implies the effect of PI on the reliability improvement of the a-Se photodetector.

References

[1] F. H. Attix. *Introduction to Radiological Physics and Radiation Dosimetry.* John Wiley, New York, 1986.

[2] C. W. E. v. Eijk. Inorganic scintillators in medical imaging. *Phys. Med. Biol.*, 2002.

[3] S. Kasap, J. B. Frey, G. Belev, O. Tousignant, H. Mani, L. Laperriere, A. Reznik, and J. A. Rowlands. Amorphous selenium and its alloys from early xeroradiography to high resolution x-ray image detectors and ultrasensitive imaging tubes. *Phys. Stat. Sol. (B)*, 2009.

[4] G. Zentai. Photoconductor-based (direct) large-area x-ray imagers. *J. Soc. Inf. Display*, 2009.

[5] M. Abkowitz. Density of states in a-se from combined analysis of xerographic potentials and transient transport data. *Philosophical Magazine Letters*, 58(1):53–57, 1988.

[6] D. M. Pai and R. C. Enck. Onsager mechanism of photogeneration in amorphous selenium. *Phys. Rev. B*, 11, 1975.

[7] Shiva Abbaszadeh. *Indirect conversion amorphous selenium photodetectors for medical imaging applications*. PhD thesis, University of Waterloo, 2013.

[8] J. U. Wallace. *Carrier Mobility in Organic Charge Transport Materials: Methods of Measurement, Analysis, and Modulation*. PhD thesis, University of Rochester, 2009.

[9] Shiva Abbaszadeh. *Charge transport in stablizied a-Se films used in X-ray image detector applications*. PhD thesis, University of Saskatchewan, 1999.

[10] S. Abbaszadeh, N. Allec, S. Ghanbarzadeh, U. Shafique, and K.S. Karim. Investigation of hole-blocking contacts for high-conversion-gain amorphous selenium detectors for x-ray imaging. *Electron Devices, IEEE Transactions on*, 59(9):2403–2409, Sept 2012.

[11] W.R. Hendee and E.R. Ritenour. *Medical Imaging Physics*. Wiley-Liss, NY, 2002.

[12] Mohammad Hadi Izadi. *Multi-mode Pixel Architectures for Large Area Real-Time X-ray Imaging*. PhD thesis, University of Waterloo, 2010.

[13] J. Yorkston and J. A. Rowlands. Flat panel detector for digital radiography. *in Handbook of Medical Imaging, J. Beutel, H. L. Kundel and R. L. Van Metter, Eds. SPIE Press*, 2000.

[14] M. Spahn. Flat detectors and their clinical applications. *European radiology*, 2005.

[15] W. Zhao and J. A. Rowlands. Large-area solid state detector for radiology using amorphous selenium. *Proc. SPIE: Medical Imaging*, 1992.

[16] D. L. Y. Lee, L. K. Cheung, and L. S. Jeromin. New digital detector for projection radiography. *Proc. SPIE: Medical Imaging*, 1995.

[17] N. Allec, S. Abbaszadeh, and K. S. Karim. Single-layer and dual-layer contrast-enhanced mammography using amorphous selenium flat panel detectors. *Phys. Med. Biol.*, 2011.

[18] N. Allec, S. Abbaszadeh, A. Fleck, O. Tousignant, and K. S. Karim. K-edge imaging using dual-layer and single-layer large area flat panel imagers. *IEEE Trans. Nucl. Sci.*, 2012.

[19] Boone J.M. Chapter 1: X-ray production, interaction, and detectin in diagnostic imaging. *in Handbook of Medical Imaging, J. Beutel, H. L. Kundel and R. L. Van Metter, Eds. SPIE Press*, 2000.

[20] E. Samei and M. J. Flynn. An experimental comparison of detector performance for direct and indirect digital radiography systems. *Med. Phys.*, 2003.

[21] R. S. Saunders Jr., E. Samei, , and C. Hoeschen. Impact of resolution and noise characteristics of digital radiographic detectors on the detectability of lung nodules. *Med. Phys.*, 2004.

[22] M. Overdick, C. Bumer, K. J. Engel, J. Fink, C. Herrmann, H. Krger, M. Simon, R. Steadman, and G. Zeitler. Status of direct conversion detectors for medical imaging with x-rays. *Nuclear Science, IEEE Transactions on*, 2009.

[23] J. Beutel, H. L. Kundel, and R. L. Van Metter. *Handbook of Medical Imaging*. SPIE Press, Bellington, 2000.

[24] C. R. Ronda. Luminescence: From theory to application. *WILEY-VCH*, 2007.

[25] M. J. Weber. Inorganic scintillators: today and tomorrow. *J. Lumin.*, 2002.

[26] B. Liu and C. Shi. Development of medical scintillator. *Chinese Sci. Bull.*, 2002.

[27] W. Zhao, D. Li, A. Reznik, B.J.M. Lui, D.C. Hunt, J.A. Rowlands, Y. Ohkawa, and K. Tanioka. Indirect flat-panel detector with avalanche gain: Fundamental feasibility investigation for sharp-amfpi (scintillator harp active matrix flat panel imager). *Medical Physics*, 2005.

[28] S.O. Kasap and J.A. Rowlands. Review x-ray photoconductors and stabilized a-se for direct conversion digital flat-panel x-ray image-detectors. *Journal of Materials Science: Materials in Electronics*, 11(3):179–198, 2000.

[29] S.O. Kasap and J.A Rowlands. Direct-conversion flat-panel x-ray image detectors. *Circuits, Devices and Systems, IEEE Proceedings*, 149(2):85–96, Apr 2002.

[30] S. O. Kasap, J. B. Frey, G. Belev, O. Tousignant, H. Mani, J. Greenspan, L. Laperriere, O. Bubon, A. Reznik, G. DeCrescenzo, K. S. Karim, and J. A. Rowlands. Amorphous and polycrystalline photoconductors for direct conversion flat panel x-ray image sensors. *Sensors*, 11(5):5112–5157, 2011.

[31] G. Lucovsky. Selenium, the amorphous and liquid states. *In The Physics of Selenium and Tellurium, E. Gerlach and P. Grosse*, 13:178–192, 1979.

[32] W. E. Spear. Transit time measurements of charge carriers in amorphous selenium films. *Proceedings of the Physical Society. Section B*, 70(7):669, 1957.

[33] S. A Mahmood and M. Z. Kabir. Dark current mechanisms in stabilized amorphous selenium based n-i detectors for x-ray imaging applications. *Journal of Vacuum Science Technology A: Vacuum, Surfaces, and Films*, 29(3):031603–031603–6, May 2011.

[34] S.O. Kasap and G. Belev. Progress in the science and technology of direct conversion x-ray image detectors: The development of a double layer a-se based detector. *Journal of Optoelectronics and Advanced Materials*, pages 1–10, 2006.

[35] H. Du, L. E. Antonuk, Y. El-Mohri, Z. Su Q. Zhao, J. Yamamoto, and Y. Wang. Investigation of the signal behavior at diagnostic energies of prototype, direct detection, active matrix, flat-panel imagers incorporating polycrystalline hgi2. *Phys. Med. Biol.*, page 132551, 2008.

[36] Robert E Johanson, S O. Kasap, J Rowlands, and B Polischuk. Metallic electrical contacts to stabilized amorphous selenium for use in x-ray image detectors. *Journal of Non-Crystalline Solids*, 227230, Part 2:1359 – 1362, 1998.

[37] E. Rosencher, V. Mosser, and G. Vincent. Transient-current study of field-assisted emission from shallow levels in silicon. *Phys. Rev. B*, 29:1135–1147, Feb 1984.

[38] K. C. Kao. *Dielectric Phenomena in Solids.* Elsevier Academic Press, San Diego, USA, 2004.

[39] S. M. Sze. *Physics of Semiconductor Devices.* Wiley, New York, USA, 1981.

[40] R. A. Street. Thermal generation currents in hydrogenated amorphous silicon p-i-n structures. *Applied Physics Letters*, 1990.

[41] R. A. Street. Long-time transient conduction in a-si:h p-i-n devices. *Philosophical Magazine B*, 1991.

[42] S. A. Mahmood and M. Z. Kabir. Modeling of transient and steady-state dark current in amorphous silicon pin photodiodes. *Current Applied Physics*, 2009.

[43] B. Polischuk, Z. Shukri, A. Legros, and H. Rougeot. Selenium direct converter structure for static and dynamic x-ray detection in medical imaging applications. *Proc. SPIE*, pages 494–504, 1998.

[44] C. Vautier, D. Carles, and C. Viger. Localized states in the gap of amorphous selenium. *International Conference on the Physics of Selenium and Tellurium*, pages 219–221, 1979.

[45] J. L. Hartke. Drift mobilities of electrons and holes and space-charge-limited current in amorphous selenium films. *Phys. Rev.*, pages 1177–1192, 1962.

[46] L. Mller and M. Mller. Current-voltage characteristics at high fields in amorphous selenium thin layers. *Journal of Non-Crystalline Solids*, 1970.

[47] M. Z. Kabir and Safayat-Al Imam. Transient and steady-state dark current mechanisms in amorphous selenium avalanche radiation detectors. *Applied Physics Letters*, 102, 2013.

[48] C. Haugen, S. O. Kasap, and J. Rowlands. Charge transport and electron-hole-pair creation energy in stabilized a-se x-ray photoconductors. *J. Phys. D: Appl. Phys.*, 32, 1999.

[49] S. O. Kasap, B. Polischuk, and D. Dodds. An interrupted field timeofflight (iftof) technique in transient photoconductivity measurements. *Review of Scientific Instruments*, 61:2080–2087, 1990.

[50] N. Mail, P. O'Brien, and G. Pang. Lag correction model and ghosting analysis for an indirect conversion flat panel imager. *J. Appl. Clin. Med. Phys.*, 8:137–146, 2007.

[51] C. Haugen, S. O. Kasap, and J. A. Rowlands. X-ray irradiation induced bulk space charge in stabilized a-se x-ray photoconductors. *J. Appl. Phys.*, pages 5495–5501, 1998.

[52] J. Kalade, E. Montrimas, and J. Rakauskas. The mechanism of sensitivity reduction in selenium layers irradiated by x-rays. *Phys. Stat. Sol. (a)*, pages 629–636, 1974.

[53] U. Schiebel, T. Buchkremer, G. Frings, and P. Quadflieg. Deep trapping and recombination in a-se:as x-ray sensitive photoreceptors. *J. Non-Cryst. Solids*, pages 216–218, 1989.

[54] W. Zhao, G. DeCrescenzo, and J. A. Rowlands. Investigation of lag and ghosting in amorphous selenium flat-panel x-ray detectors. *Proc. SPIE*, 4682:9–20, 2002.

[55] G. Juka and K. Arlauskas. Impact ionization and mobilities of charge carriers at high electric fields in amorphous selenium. *Phys. Stat. Sol. (a)*, 59:389–393, 1980.

[56] G. Juka and K. Arlauskas. Feature of hot carriers in a-se. *Phys. Stat. Sol. (a)*, 77:387–391, 1983.

[57] O. Rubel, S. D. Baranovskii, I. P. Zvyagin, P. Thomas, and S. O. Kasap. Lucky-drift model for avalanche multiplication in amorphous semiconductors. *Phys. Stat. Sol. (c)*, 1, 2004.

[58] K. Tanioka, J. Yamazaki, K. Shidara, K. Taketoshi, T. Kawamura, S. Ishioka, and Y. Takasaki. An avalanche-mode amorphous selenium photoconductive layer for use as a camera tube target. *IEEE Electron Device Lett.*, 8:392–394, 1987.

[59] G. Belev and S. O. Kasap. Reduction of the dark current in stabilized a-se based x-ray detectors. *J. Non-Cryst. Solids*, pages 1616–1620, 2006.

[60] B. T. Polischuk, P. Leblanc, M. Choquette, Z. A. Shukri, and H. M. Rougeot. Direct conversion digital x-ray detector with inherent high voltage protection for static and dynamic imaging. *U.S. Patent*, 2002.

[61] G. Belev. *Electrical properties of amorphous selenium based photoconductive devices for application in x-ray image detector*. PhD thesis, University of Saskatchewan, 2007.

[62] L. Cheung, S. Bogdanovich, E. Ingal, and C. L. Williams. Amorphous selenium flat panel x-ray imager for tomosynthesis and static imaging. *U.S. Patent*, 200t.

[63] S. Abbaszadeh, C. C. Scott, O. Bubon, A. Reznik, and K. S. Karim. Enhanced detection efficiency of direct conversion x-ray detector using polyimide as hole-blocking layer. *Scientific Reports*, 2013.

[64] B. Ruhstaller, E. Knapp, B. Perucco, N. Reinke, D. Rezzonico, and F. Mller. Opto-electronic devices and properties. *InTech*, 2011.

[65] H. Scher and E. Montroll. Anomalous transit-time dispersion in amorphous solids. *Physical Review B*, 1975.

[66] Tabak W.D. and Warter P.J. Field-controlled photogeneration and free carrier transport in amorphous selenium films. *Physical Review*, 1968.

[67] Papadakis A.C. Theory of space-charge perturbed currents in insulators. *Journal of Physics and Chemistry of Solids*, 1967.

[68] M. Abkowitz and D. M. Pai. Photoelectronic behavior of a-se and some a-se: As alloys in their glass transition regions. *Phys. Rev. B*, 1978.

[69] K. Kikuchi, Y. Ohkawa, K. Miyakawa, T. Matsubara, K. Tanioka, M. Kubota, and N. Egami. Hole-blocking mechanism in high gain avalanche rushing amorphous photoconductor (harp) film. *Phys. Stat. Sol. (C)*, 2011.

[70] N. R. Tu and K. C. Kao. High-field electrical conduction in polyimide films. *J. Appl. Phys.*, 1999.

[71] O. Bubon, G. DeCrescenzo, W. Zhao, Y. Ohkawa, K. Miyakawa, T. Matsubara, K. Kikuchi, K. Tanioka, M. Kubota, J. A. Rowlands, and A. Rezik. Electroded avalanche amorphous selenium (a-se) photosensor. *Curr. Appl. Phys.*, 2012.

[72] V. V. Mikla V. I Mikla. *Medical Imaging Technology*. Elsevier, Oxford, 2014.

[73] Abkowitz M. and Enck R. C. Xerographic spectroscopy of gap states in amorphous semiconductors. *Phys. Rev. B*, 1982.

[74] K. Tsuji, Y. Takasaki, T. Hirai, and K. Taketoshi. Impact ionization process in amorphous selenium. *J. Non-Cryst. Solids*, 1989.

[75] Hirotaka Watano et al. Development of high-image quality and high-durability direct conversion. digital radiography system fdr acselerate. *Fuji film report*, 2009.

[76] Z. Shukri and H. Rougeot. Selenium alloys with improved stability for digital x-ray detector applications. *Proc. SPIE*, 1999.

[77] K. Ogusu, O. Nakane, Y. Igasaki, Y. Okamura, S. Yamada, and T. Hirai. Advanced a-se film with high sensitivity and head-resistance for x-ray detectors. *Proc. SPIE*, 2009.

[78] F. Nariyuki, S. Imai, H. Watano, T. Nabeta, and Y. Hosoi. New development of large-area direct conversion detector for digital radiography using amorphous selenium with c60-doped polymer layer. *Proc. SPIE*, 2010.

[79] B. A. Weinstein, R. E. Tallman, G. P. Lindberg, J. A. Rowlands, A. Reznik, M. Kubota, and K. Tanioka. Photocrystalization in a-se film with and without as-se buffer layers. *APS Bull. Amer. Phys. Soc.*, 2011.

[80] C. P. Wong. *Polymers for Electronic and Photonic Application.* Academic Press, San Diego, 1993.